





# Rotation curves and dynamical masses of MaNGA barred galaxies

Eduardo O. Schmidt <sup>1,2,3</sup>★, Damián Mast <sup>1,2</sup>, Gaia Gaspar <sup>1,2</sup> and Walter Weidmann <sup>1,2</sup>

<sup>1</sup>*Observatorio Astronómico de Córdoba, Universidad Nacional de Córdoba, Laprida 854, Córdoba, Argentina.*

<sup>2</sup>*Consejo de Investigaciones Científicas y Técnicas de la República Argentina, Buenos Aires, Argentina.*

<sup>3</sup>*Instituto de Astronomía Teórica y Experimental (IATE), CONICET-UNC, Laprida 854, Córdoba, Argentina*

Accepted XXX. Received YYY; in original form ZZZ

## ABSTRACT

In this paper we analyze a sample of 46 barred galaxies of MaNGA. Our goal is to investigate the stellar kinematics of these galaxies and obtain their rotation curves. Additionally, we aim to derive the total stellar and dynamical masses, as well as the maximum rotation velocity, in order to examine their distributions and scaling relations.

Using the Pipe3D dataproducts publicly available we obtained the rotation curves, which were fitted considering two components of an axisymmetric Miyamoto–Nagai gravitational potential.

We found a wide range of the maximum rotation velocities ( $117\text{--}340\text{ km s}^{-1}$ ), with a mean value of  $200\text{ km s}^{-1}$ . In addition we found that the total stellar and dynamical masses are in the range of  $\log(M_{\text{star}}/M_{\odot}) = 10.1\text{--}11.5$ , with a mean value of  $\log(M_{\text{star}}/M_{\odot}) = 10.8$ , and  $\log(M_{\text{dyn}}/M_{\odot}) = 10.4\text{--}12.0$ , with a mean value of  $\log(M_{\text{dyn}}/M_{\odot}) = 11.1$ , respectively. We found a strong correlation between dynamical mass and maximum velocity, between maximum velocity and magnitude, and between stellar mass and maximum velocity. According to these results, barred galaxies exhibit similar behaviour to that of normal spiral galaxies with respect to these relations, as well as in terms of the distribution of their dynamical mass and maximum rotation velocity. However, we found that the distribution of stellar masses of barred galaxies is statistically different from other samples including non-barred galaxies. Finally, analyzing the galaxies that show nuclear activity, we find no difference with the rotation curves of normal galaxies.

**Key words:** galaxies: kinematics and dynamics – galaxies: spiral – galaxies: structure

## 1 INTRODUCTION

Rotation curves (RCs) are the main tracers of the distribution of mass in spiral galaxies (e.g., Ashman 1992; Persic & Salucci 1995; Sofue & Rubin 2001; Kalinova et al. 2017a). As such, they represent the major tool for determining the mass distribution, providing fundamental information for understanding the evolution, dynamics, and formation of spiral galaxies (e.g., Persic & Salucci 1995; Sofue et al. 1999; Sofue & Rubin 2001; Martínez-Medina et al. 2020).

There are typical kinematic tracers for galaxies which include stars (e.g., Bekeraité et al. 2016a,b; Kalinova et al. 2017a,b; Yoon et al. 2021) and ionised, atomic or molecular gas (e.g., Levy et al. 2018). In this context, astronomers have at their disposal several observing techniques and methods for determining rotation curves and velocity fields for both gas and stars (Falcón-Barroso et al. 2017; García-Lorenzo et al. 2015). For example, traditional long slit spectroscopy, Fabry-Perot spectrographs, or integral field instruments are often used for these purposes (see for example the review of Sofue & Rubin 2001). With the advent of large integral-field spectroscopic (IFS) surveys such as CALIFA (Alto Legacy Integral Field Area, Sánchez et al. 2012), SAMI (Sydney-AAO (Australian Astronomical Observatory) Multi-object IFS, Croom et al. 2012), or MaNGA (Mapping Nearby Galaxies at Apache Point Observatory, Bundy et al. 2015),

the possibility of carrying out detailed studies with samples covering wide ranges of parameters has become a reality. Rotation curves can be obtained by measuring spectroscopic emission lines such as  $H\alpha$ , [OIII], [NII], [SII], HI, and CO lines and stellar absorption lines such as the generated by Ca, H, He, K, Mg, Na, among other chemical elements, and techniques vary from single line to full spectrum fitting (Cappellari & Emsellem 2004; Cappellari 2017; Sánchez et al. 2016a).

Each of the different tracers has its difficulties when studying and analyzing them (e.g., Leung et al. 2018; Martínez-Medina et al. 2020), in addition to preferentially tracing different components in the galaxy. For example, the gas kinematic has an intrinsic turbulent nature and therefore gas velocity fields are complex (e.g., Barrera-Ballesteros et al. 2014). Particularly, the CO molecule emission is considered to be a good tracer of the circular velocity of disc galaxies, however the typical presence of bars and spiral arms clearly influences the molecular gas orbits, making them turbulent (e.g., Laine et al. 1999; Shetty et al. 2007). In this context, although stellar kinematics can present higher velocity dispersion, stellar velocity fields are less distorted than gas fields (e.g., Adams et al. 2012; Bekeraité et al. 2016a). However, stellar kinematics presents its complications when it comes to deriving properties. Leung et al. (2018) studied and analyzed three dynamical models used to calculate masses from stellar dynamics, which are the Jeans method, the asymmetric drift correction method, and the Schwarzschild model method. These au-

★ E-mail: eduardo.schmidt@unc.edu.ar

thors found that the three models can reproduce the CO circular velocity at 1 effective radius to within 10%. The scatter in the inner regions can be of  $\sim 20\%$ , because some assumptions may break down (see [Leung et al. 2018](#), for more details). These authors found that all three models can recover the dynamical mass at 1 effective radius better than 20%. For their part, [Martinsson et al. \(2013\)](#) studied [OIII] $\lambda 5007$  and stellar kinematics of 30 nearby spiral galaxies and found that the [OIII] and stellar rotation curves exhibit signatures of asymmetric drift with a rotation difference that is 11% of the maximum rotation speed of the galaxy disk.

It is clear that a sufficiently complete view of the mass distribution in a galaxy can only be achieved through the use of different tracers. Moreover, understanding the scope and drawbacks, not only of the tracers but also of the limitations of the observational techniques used for each of the measurements, is a fundamental step in our understanding of the mass distribution in galaxies. Thus, having independent mass determinations for homogeneous samples of galaxies that allow us to compare analysis methods and even observational regimes (such as low spatial resolution and spectroscopic observations) is a fundamental building block in the study of galaxy dynamics and evolution in this new era of large integral field spectroscopy galaxy surveys.

In this work, we study the stellar kinematics of barred galaxies to obtain stellar rotation curves that are less affected by the turbulent motions more characteristic of gas kinematics. We intend to avoid the volatility inherent to gas curves that are generated by any perturbation. This way, we aim to analyze the stellar kinematic and derive the stellar rotation curves of a sample of MaNGA barred galaxies.

Several papers in the literature investigate and present RCs using different methods. For example, [Mathewson et al. \(1992\)](#) study the RCs of 965 southern spiral galaxies through  $H\alpha$  and HI emission. [Makarov et al. \(2001\)](#) present RCs of 135 edge-on galaxies through  $H\alpha$  and [Vogt et al. \(2004a,b\)](#) study rotation curves of 329 spiral galaxies using  $H\alpha$  and HI emission. In addition, [Márquez et al. \(2002\)](#) derive rotation curves of 111 galaxies through  $H\alpha$  and [Spano et al. \(2008\)](#) study rotation curves of 36 galaxies through HI emission. For their part, [Lang et al. \(2020\)](#) present RCs of 67 galaxies (including 45 barred galaxies) through CO emission. Moreover, [Martinsson et al. \(2013\)](#) determined the ionized-gas ([OIII] $\lambda 5007$ ) and stellar rotation curves of a sample of 30 nearby spiral galaxies and [Hernandez et al. \(2005\)](#) present the  $H\alpha$  gas kinematics of 21 barred spiral galaxies. In addition, [Bekeraïté et al. \(2016a\)](#) study the stellar rotation curves of 199 rotating galaxies and [Kalinova et al. \(2017b\)](#) present the stellar rotation curves of 238 galaxies. Moreover, [Di Teodoro et al. \(2023\)](#) present the HI rotation curves of 15 massive spiral of the local universe and [Kalinova et al. \(2017a\)](#) study the stellar rotation curves of 18 late type spirals. [Yoon et al. \(2021\)](#) analysed the shape of the RCs of the MaNGA data release. In general, the aims of those works vary from testing the cold dark matter (CDM) models of galaxy formation to analyzing scaling relations. In any case, it is important to have homogeneously observed and analyzed dataset. In this context, one of the main goals of this work is to study the stellar kinematic and obtain the stellar rotation curves of a sample of 46 barred galaxies, and then, by fitting these RCs, derive the dynamical masses of an homogeneous galaxy sample.

There are different methods for determining dynamical masses of spiral galaxies. For example, [Aquino-Ortíz et al. \(2020\)](#) use the stellar kinematics for galaxies from MaNGA to explore a universal fundamental plane and the relation between the dynamical and stellar masses. In this scenario, RCs constitute an independent method for determining the dynamical masses of spiral galaxies (e.g., [Burbidge et al. 1959, 1961](#); [Rubin et al. 1964](#); [Krumm & Salpeter 1977](#); [Pence](#)

[1981](#); [Agüero et al. 2004](#); [Jalocha et al. 2010](#); [Daod & Zeki 2019](#)). As we mentioned above, obtaining the total dynamical mass of the sample of barred spiral galaxies by analyzing their stellar rotation curves, represents a valuable contribution to the study of galaxy dynamics.

Even though barred galaxies constitute  $\sim 50\%$  of all disk galaxies (e.g., [Marinova & Jogee 2007](#); [Sheth et al. 2008](#); [Agueri et al. 2009](#)), they have been observed and studied less than non-barred galaxies in part due to their kinematic complexity. However, although the kinematic study of barred galaxies can be more difficult than for non-barred galaxies because their gas tracers are very in-homogeneously distributed on small scales (e.g., [Bosma 1996](#)), the large-scale properties of the rotation curves of barred galaxies are generally similar to those of non-barred galaxies (e.g., [Sofue & Rubin 2001](#)).

This paper is organized as follows. Sect. 2 presents the sample of barred spiral galaxies and the data we worked with. Sect. 3 describes the procedure by which the velocity fields and radial velocity curves were obtained. In Sect. 4 we present our results, i.e., the process of obtaining and fitting the rotation curves, the derivation of the dynamical and stellar masses of the galaxies, and the study of the scaling relations. In Sect. 5 we make a comparison between our results and those of the literature. Finally, in Sect. 6 we provide a brief summary of the work and make final remarks.

## 2 SAMPLE

For our study, we selected the galaxy sample analysed by [Guo et al. \(2019\)](#), which consists of barred galaxies from MaNGA. This survey investigates the internal structure and composition of gas and stars in a sample of  $\sim 10000$  galaxies of the nearby universe (for more details of the project see [Bundy et al. 2015](#)). We used the integral field unit (IFU) spectroscopic data taken at the 2.5 m Sloan Telescope ([Gunn et al. 2006](#)), which has 1423 fibres with  $2''$  core diameters over a  $3''$  diameter field of view.

The sample studied by [Guo et al. \(2019\)](#) is made up of 53 plate-IFU observations. Note that plates IFU 8256–6101 and 8274–6101 correspond to the galaxy SDSS J105456.35+412954.3 and plates 8588–3701 and 8603–12701 correspond to SDSS J163233.73+390751.7. In addition, we excluded from the analysis the galaxies SDSS J154702.69+542027.1, SDSS J162200.73+493114.8, SDSS J164029.54+391406.3 and SDSS J162907.83+403954.1 (plate-IFU: 8481–12701, 8482–12703, 8601–12705, and 8603–12703, respectively) which have a noisy velocity map. Moreover, as we will see below (Sect. 4) one galaxy (SDSS J090641.14+412154.3, plate-IFU 8247–3701) was rejected from the analysis because the dispersion of velocities dominates its entire curve compared with the rotation velocity. This way, our final sample consists of 46 barred galaxies. Table 1 lists the main parameters of the galaxy sample, such as the MaNGA ID, the galaxy name, right ascension (J2000), declination (J2000), morphological type, absolute r-band magnitude from SDSS-DR9 ([Ahn et al. 2012](#)), effective radius in the r-band from SDSS-DR9, redshift, galaxy inclination, galaxy kinematic PA and systemic velocity. All data were taken from [Guo et al. \(2019\)](#), except the galaxy name (column 2), which has been taken from the Sloan Digital Sky Survey (SDSS) IV DATA Release 13 ([Albareti et al. 2017](#)) and the systemic velocity (column 11), which has been obtained in this work (Sect. 3). The galaxy inclination was measured from the ellipticity radial profile using ellipse fitting of r-band SDSS image, while the galaxy kinematic PA was measured from the ve-

locity map using `fit_kinematic_pa.py`<sup>1</sup> code (see Guo et al. 2019, for more details). In addition, we have made use of the Nasa Extragalactic Database (NED)<sup>2</sup> to verify galaxy parameters such as the radial velocity.

In order to make the characterisation of the sample more comprehensive, in Fig. 1 we present the redshift and r-band magnitude distributions for our sample of galaxies (left and right panels, respectively). The redshift of the entire sample ranges from 0.0228 to 0.1303 and has a distribution with a mean value of  $z = 0.0399$ , a standard deviation of 0.019 and an interquartile range (IQR) of 0.021. There is one object with  $z \sim 0.13$ , while the remaining galaxies (98 % of the sample) have redshifts in the range 0.0228 – 0.0753. By removing this object from the analysis, the redshift distribution would have a standard deviation of 0.0138. Regarding the magnitude, it ranges from  $-22.89$  to  $-19.77$ , with a mean value of  $-21.33$  and a distribution with a standard deviation of 0.82 and an IQR of 1.16. Both distributions show that the galaxy sample is homogeneous in both redshift and magnitude.

### 3 PROCEDURE

The data included in this paper are from Sloan Digital Sky Survey (SDSS) IV DATA Release 13<sup>3</sup> (Albareti et al. 2017). We used the publicly available dataproducs obtained by Pipe3D (Sánchez et al. 2016b, 2018a). From these cubes we extracted the V-band pseudo-image, the stellar radial velocity field, and the error in the stellar radial velocity determination for each spaxel. Using MARVIN software (Cherinka et al. 2019) we also obtained the SDSS color image with the indicated IFU MaNGA FoV for comparison with the cube maps. The pseudo V-image was used to determine the peak emission and the systemic velocity. From the kinematic position angle ( $PA_{Kin}$ ) determined by Guo et al. (2019) we carried out an extraction of the radial velocities in a 1 spaxel width pseudo-slit. This allowed us to construct the stellar radial velocity curves. Errors were estimated from the error plane in MaNGA datacubes. We used the value of the radial velocity error indicated in the Pipe3D maps for each spaxel. A typical error bar is indicated in the plots. In the upper panels of Fig. A1 we show the SDSS images, the pseudo V-images, and the stellar radial velocity fields for each galaxy.

For the choice of the systemic velocity ( $V_{sys}$ ) for each galaxy, the velocities corresponding to the peak of the pseudo-image obtained in the V-band were compared with the velocity that best symmetrizes the radial velocity curve. This comparison is performed to analyze possible off-centering of the velocity fields with the luminosity distribution, but in all cases the displacements were less than 2 arcsec, which implies that they are within the spatial resolution element. Thus the  $V_{sys}$  adopted are those that best symmetrize the radial velocity curves. In all cases these  $V_{sys}$  are in agreement with the values found in the literature and in the NED.

## 4 RESULTS

### 4.1 The rotation curves

Once the radial velocity curves are determined, the rotation velocity ( $V_{rot}$ ) can be calculated as:

$$V_{rot} = \frac{V_{obs} - V_{sys}}{\sin(i)} \quad (1)$$

where  $V_{obs}$  is the observed radial velocity,  $V_{sys}$  is the systemic radial velocity and  $i$  is the galaxy inclination.

In order to fit all the RCs, we made use of `galpy`<sup>4</sup> (Bovy 2015), which is a Python package for galactic dynamics. For this, we considered two mass components corresponding to axisymmetric Miyamoto–Nagai gravitational potentials (Miyamoto & Nagai 1975):

$$\Phi(R, z) = -\frac{GM}{\sqrt{R^2 + [a + \sqrt{z^2 + b^2}]^2}} \quad (2)$$

where  $\Phi(R, z)$  is the Miyamoto–Nagai potential at  $(R, z)$  position,  $a$  and  $b$  are shape parameters and  $M$  is the total mass. By way of example, the ratio  $b/a \sim 0.4$  corresponds to a flattened disk distribution,  $b/a = 1$  to an ellipsoidal distribution and  $b/a \sim 5$  to a spherical distribution (e.g., Binney & Tremaine 1987).

Given its simplicity, the Miyamoto–Nagai potential is one of the most widely used models for fitting rotation curves (e.g., Binney & Tremaine 1987; Sofue 2017; Granados et al. 2017; Ciotti 2021, 2022). It is a generalisation of the Plummer’s spherical potential (when  $a = 0$ ) and the Kuzmin’s potential of a razor-thin disk (when  $b = 0$ ). This way, depending on the values of the two parameters  $a$  and  $b$ , the Miyamoto–Nagai model can represent the potential of anything from an infinitesimally thin disk to a spherical distribution (see for example Binney & Tremaine 1987, for more details).

From the centrifugal-equilibrium condition, the rotation velocity in the equatorial plane is related to the gravitational potential  $\Phi(R, z=0)$  in the form:

$$V_{rot}(R) = \sqrt{-R(\partial\Phi/\partial R)} \quad (3)$$

Taking into account Eq. 2 and Eq. 3, the rotation velocity in the galactic plane at  $z = 0$  is given by:

$$V_{rot}(R) = R \sqrt{\frac{GM}{[R^2 + (a + b)^2]^{3/2}}} \quad (4)$$

The fitting of the rotation curves was carried out in a two-stage procedure. The first thing we did was to perform a least squares fit to the data in order to have a first approximation. However, an automatic fit may consider regions where there are non-circular motions generated by nonaxisymmetric disturbances and thus affect the global fit that takes into account rotation velocities. Because of this, we carefully checked each curve individually, and using the least square fit as a reference, we made use of `galpy` improving each fit by making it take into account only the observed rotation motions, which are representative of the gravitational potential. This procedure was carried out varying the input parameters mass,  $a$ , and  $b$  and considering

<sup>1</sup> <https://www-astro.physics.ox.ac.uk/~cappellari/software/>

<sup>2</sup> The NASA/IPAC Extragalactic Database (NED) is operated by the Jet Propulsion Laboratory, California Institute of Technology, under contract with the National Aeronautics and Space Administration.

<sup>3</sup> [https://data.sdss.org/sas/dr13/manga/spectro/redux/v1\\_5\\_4/](https://data.sdss.org/sas/dr13/manga/spectro/redux/v1_5_4/)

<sup>4</sup> <http://github.com/jobovy/galpy>

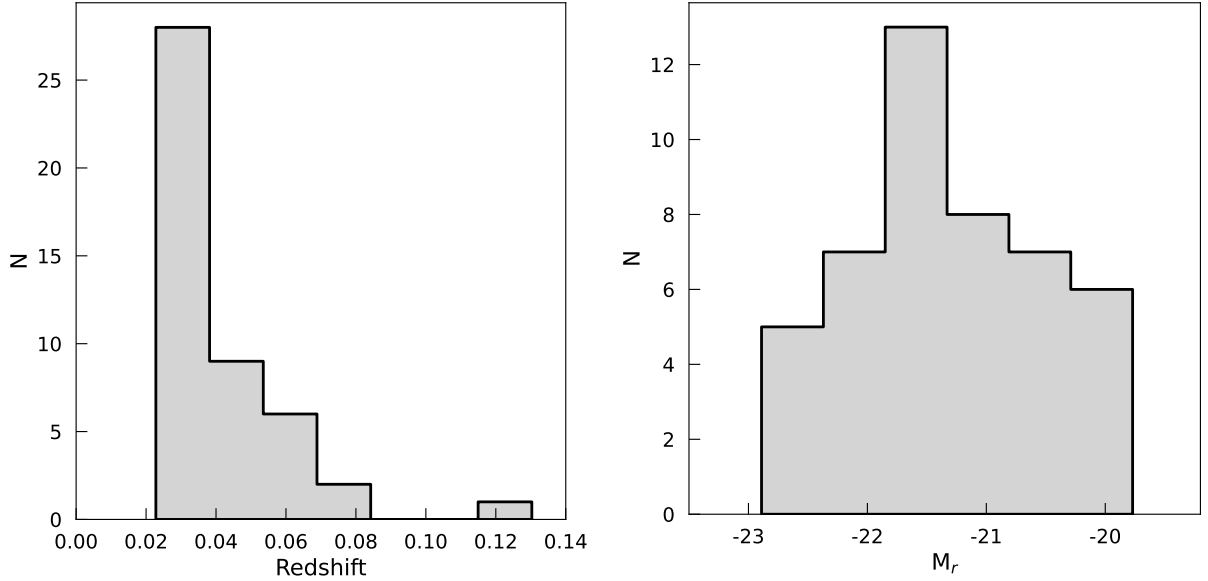


**Figure 1.** Redshift and r-band magnitude distributions for the galaxies of our sample are shown in the left and right panels, respectively. The data of both plots were taken from [Guo et al. \(2019\)](#).

each galaxy individually to ensure the best fit, which has been carefully inspected by eye. To determine the uncertainties of the fits, we repeated the measurement procedure 15 times for all galaxies. We assumed that any errors are given by the dispersion in the distribution of these measurements, considering them at  $1\sigma$ . Concerning the fits, relative errors in the velocity are in the range 3% – 8%. These errors take into account only our measurements procedures, and do not involve other factors such as the observation process, reduction or calibrations.

All galaxies of the sample were fitted considering the presence of two galactic subsystems: a central ellipsoidal component and a flattened disk, in agreement with previous works that also have fitted rotation curves of barred spiral galaxies (e.g., [Díaz et al. 1999](#); [Agüero et al. 2004](#); [Schmidt et al. 2019](#)).

Given the morphological characteristics of this sample, a significant fraction of the galaxies are late type objects (see Table 1). Related to this and considering the rotation curve fitting, the central component is almost absent or negligible compared to the disk component in all but a few galaxies (see for example the fits of 7495–12704 and 7962–12703, among others, in Fig. A1). Although for consistency in all the fittings the two components were kept. In none of the fits a third component corresponding to the halos was used, on the one hand because the fit was satisfactory with two components and on the other hand because the scale radius of the halo is larger than the radii involved in our data (e.g., [Sofue 2016](#)). Related to this, it has to be noted that the possible gravitational influence of a dark matter halo may be implied by the disc component. However, in this work we do not intend to physically interpret the different components separately, but consider the total fit of the rotation curve that will allow us to robustly calculate the dynamical masses of the galaxies of the sample (see Sect. 4.2).

In order to check for the reliability of the rotation curves as dynamical mass estimators, we follow the procedure used by [Kalinova et al. \(2017a\)](#) and [Bekeraité et al. \(2016a\)](#). This procedure considers that when the ordered-over-random motion  $V\phi/\sigma_R < 1.5$ , the rotation curve might not be a reliable tracer. To do this, we made use of the

dispersion maps available as part of the Pipe3D dataproducts to construct the dispersion velocity radial profiles to evaluate the  $V\phi/\sigma_R$  ratio. We performed this test for all galaxies in our sample. As we said in Sect. 2, we rejected one galaxy (SDSS J090641.14+412154.3, plate-IFU 8247-3701) whose entire extension presents an important contribution of the stellar velocity dispersion compared with the rotation velocity. This way, our whole sample is constituted by galaxies whose dynamic is dominated by rotation. Considering that practically all the galaxies in our sample present a negligible bulge component, and in order to make an homogeneous treatment to our data and to avoid any potentially incorrect assumption, we will study the stellar kinematic of the galaxies neglecting the correction methods mentioned in Sect. 1 (e.g., [Bureau & Carignan 2002](#); [Di Teodoro et al. 2021, 2023](#)).

Table B1 lists the obtained parameters of our fits, such as the scale parameters, the mass of each galactic subsystem and the total mass. Fig. A1 presents all the fitted rotation curves of the galaxy sample. In addition, Fig. 2 shows the distribution of the maximum rotation velocity, i.e., the highest rotation velocity measured over each rotation curve. According to our results, the maximum rotation velocities show a wide range, with values from 117 to 340  $\text{km s}^{-1}$ , with most of the objects showing a maximum rotation velocity in the range  $\sim 120$ –250  $\text{km s}^{-1}$ . The distribution has a mean value of 200  $\text{km s}^{-1}$ , a standard deviation of 50  $\text{km s}^{-1}$  and an IQR of 57. These values are in agreement with previous results on spiral galaxies (e.g., [Persic & Salucci 1995](#); [Sofue & Rubin 2001](#); [Agüero et al. 2004](#); [Sofue 2017](#); [Schmidt et al. 2019](#); [Martinez-Medina et al. 2020](#), among others). There are 11 galaxies from our sample (7495-12704, 8137-9102, 8257-6101, 8318-12703, 8330-12703, 8335-12701, 8439-12702, 8452-12703, 8482-12705, 8549-12702 and 8601-12705) that were also studied by [Pilyugin et al. \(2019\)](#), who obtained rotation curves through the analysis of the  $H\alpha$  velocity field. In general, the rotation velocities determined in this work are in good agreement with the results reported in the mentioned paper. There are, however, some differences in the rotation velocities of a few galaxies. These differences may probably be due to the procedure used to construct the rotation curves, the



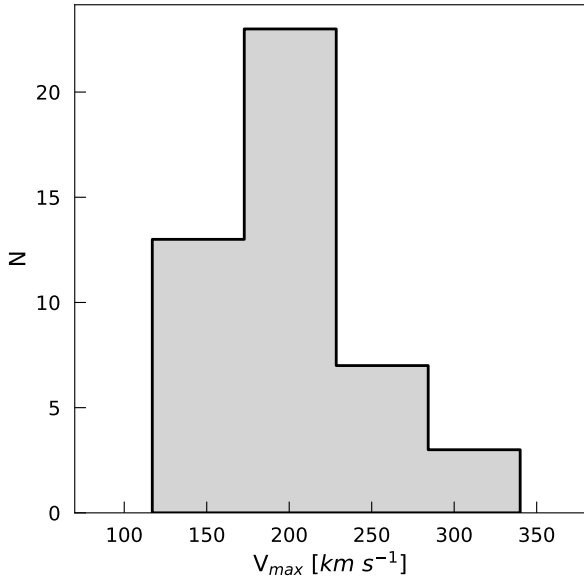
**Table 1.** The sample of 46 barred galaxies. Columns: (1) MaNGA ID; (2) galaxy name; (3) right ascension (J2000); (4) declination (J2000); (5) morphological type; (6) absolute r-band magnitude from SDSS-DR9; (7) effective radius in the r-band from SDSS-DR9; (8) redshift; (9) galaxy inclination; (10) galaxy kinematic PA; (11) systemic velocity. All data were taken from [Guo et al. \(2019\)](#), except the galaxy name (from the SDSS DR13) and the systemic velocity (Sect. 3).

Plate IFU	Galaxy name	RA (°)	DEC (°)	Morph.	Mr (mag)	$R_e$ (")	$z$	$i$ (°)	$PA_{kin}$ (°)	$V_{syst}$ (km s <sup>-1</sup> )
(1)	(2)	(3)	(4)	(5)	(6)	(7)	(8)	(9)	(10)	(11)
7495–12704	SDSS J134145.21+270016.9	205.4384	27.0048	SBbc	−21.40	8.65	0.0289	52.2±0.6	173.0±0.6	8768
7962–12703	SDSS J172452.14+280441.8	261.2173	28.0783	SBab	−22.33	8.34	0.0477	61.2±1.2	37.0±0.9	14452
7990–3704	SDSS J172817.97+564629.2	262.0749	56.7748	SB0	−20.15	3.83	0.0291	39.4±1.4	15.2±3.4	8800
7990–9101	SDSS J171901.32+571024.6	259.7555	57.1735	SBc	−19.77	4.51	0.0280	71.8±0.2	20.0±3.8	8488
7992–6104	SDSS J170107.08+644036.6	255.2795	64.6769	SBc	−20.31	8.78	0.0271	46.7±1.8	6.0±2.8	8188
8082–6102	SDSS J031947.01+003504.4	49.9459	0.5846	SB0	−21.46	6.91	0.0242	41.3±0.5	99.0±0.9	7346
8083–6102	SDSS J032427.59−000510.8	51.1150	−0.0863	SBa	−21.62	4.70	0.0365	70.4±0.2	62.8±0.9	11028
8083–12704	SDSS J032247.22+000857.6	50.6968	0.1494	SBbc	−21.03	13.32	0.0228	41.7±0.9	167.0±1.4	6946
8133–3701	SDSS J072819.02+431807.5	112.0793	43.3021	SBb	−20.10	2.39	0.0437	44.6±1.1	102.8±3.5	13159
8134–6102	SDSS J073941.88+455445.4	114.9245	45.9126	SB0a	−21.40	5.98	0.0320	53.8±0.9	93.0±0.8	9670
8137–9102	SDSS J074809.26+433526.4	117.0386	43.5907	SBb	−21.07	6.68	0.0311	43.3±2.2	132.8±1.9	9417
8140–12701	SDSS J074743.27+412310.9	116.9303	41.3864	SBa	−20.61	5.69	0.0286	37.8±1.3	62.8±1.8	8674
8140–12703	SDSS J075135.62+425248.3	117.8985	42.8801	SBb	−21.87	9.85	0.0320	55.0±0.6	28.0±1.1	9652
8243–6103	SDSS J083641.96+534338.0	129.1749	53.7272	SB0	−21.65	4.75	0.0315	59.1±0.6	9.8±0.6	9526
8244–3703	SDSS J084758.26+513603.6	131.9928	51.6010	SB0	−21.03	2.50	0.0483	46.1±1.1	71.5±1.6	14561
8249–6101	SDSS J091014.98+461735.8	137.5625	46.2933	SBc	−20.27	4.64	0.0267	48.7±1.4	63.5±1.6	8092
8254–9101	SDSS J104502.80+434217.0	161.2617	43.7048	SBa	−21.78	8.00	0.0253	44.1±1.6	27.2±0.8	7698
8256–6101	SDSS J105456.35+412954.3	163.7348	41.4985	SBa	−20.79	6.06	0.0246	51.4±2.6	134.0±0.9	7492
8257–3703	SDSS J110637.35+460219.6	166.6557	46.0388	SBb	−20.34	4.03	0.0250	58.3±0.6	155.2±1.2	7543
8257–6101	SDSS J110102.71+445317.7	165.2613	44.8882	SBc	−20.86	5.77	0.0294	45.0±2.2	159.2±1.5	8904
8312–12702	SDSS J162105.00+395502.6	245.2709	39.9174	SBc	−21.24	7.23	0.0320	42.9±1.1	95.2±1.8	9698
8312–12704	SDSS J162912.98+410903.1	247.3041	41.1509	SBb	−21.00	7.47	0.0296	46.1±0.7	34.0±1.8	8977
8313–9101	SDSS J155847.40+415617.1	239.6975	41.9381	SBb	−21.87	6.76	0.0387	38.6±0.7	110.5±1.0	11685
8317–12704	SDSS J125448.95+440920.1	193.7040	44.1556	SBa	−22.68	7.14	0.0543	69.2±0.3	101.8±0.9	16355
8318–12703	SDSS J130455.76+473013.0	196.2324	47.5036	SBb	−22.21	9.09	0.0393	61.8±0.9	53.8±0.9	11869
8320–6101	SDSS J134630.60+224221.6	206.6275	22.7060	SBb	−20.37	5.22	0.0266	50.0±0.6	5.0±1.1	8046
8326–3704	SDSS J141924.05+455402.8	214.8502	45.9008	SBa	−20.25	3.83	0.0265	50.4±1.1	159.8±3.0	8039
8326–6102	SDSS J142004.29+470716.8	215.0179	47.1213	SBb	−22.06	2.95	0.0704	51.9±0.9	145.8±1.6	21156
8330–12703	SDSS J133329.90+403146.8	203.3746	40.5297	SBbc	−20.67	7.51	0.0269	45.0±0.5	68.5±1.9	8143
8335–12701	SDSS J142134.86+402129.1	215.3953	40.3581	SBb	−21.66	4.39	0.0633	67.0±0.5	78.2±1.4	19096
8439–6102	SDSS J093106.75+490447.1	142.7782	49.0797	SBab	−21.64	4.54	0.0339	49.3±0.5	45.5±1.1	10229
8439–12702	SDSS J092609.43+491836.7	141.5393	49.3102	SBa	−21.57	8.10	0.0269	55.1±0.4	31.5±0.5	8167
8440–12704	SDSS J090434.15+412352.1	136.1423	41.3978	SBb	−21.12	4.56	0.0270	57.9±0.4	150.0±0.8	8201
8447–6101	SDSS J134431.98+401424.0	206.1333	40.2400	SBb	−22.89	4.48	0.0753	63.9±0.8	178.2±1.2	22661
8452–3704	SDSS J103009.35+471642.2	157.5390	47.2784	SBc	−19.97	4.34	0.0251	59.7±0.3	72.0±2.5	7597
8452–12703	SDSS J102713.35+481441.2	156.8057	48.2448	SBb	−22.83	8.13	0.0610	45.7±2.4	65.0±1.2	18356
8482–9102	SDSS J102713.35+481441.2	242.9559	49.2287	SBb	−21.59	3.54	0.0580	62.6±0.6	63.8±1.9	17493
8482–12705	SDSS J161652.00+501655.8	244.2167	50.2822	SBb	−22.06	7.39	0.0417	63.0±1.0	117.0±1.0	12583
8486–6101	SDSS J155209.48+461911.2	238.0396	46.3198	SBc	−21.57	3.56	0.0589	40.4±1.2	113.5±1.4	17734
8548–6102	SDSS J162205.36+463726.9	245.5224	46.6242	SBc	−20.83	3.85	0.0478	54.1±0.4	58.8±3.6	14386
8548–6104	SDSS J162259.35+464031.2	245.7474	46.6753	SBc	−20.47	2.73	0.0480	62.2±1.6	120.2±5.0	14465
8549–12702	SDSS J160505.14+452634.7	241.2714	45.4430	SBb	−22.03	6.72	0.0433	54.3±2.6	100.8±1.0	13084
8588–3701	SDSS J163233.73+390751.7	248.1406	39.1310	SBb	−22.88	4.43	0.1303	40.4±1.7	136.2±1.9	39164
8604–12703	SDSS J163103.40+395018.5	247.7642	39.8385	SBab	−21.67	9.08	0.0305	48.8±1.0	97.8±1.0	9254
8612–6104	SDSS J170001.67+384857.7	255.0069	38.8160	SBb	−21.83	8.60	0.0356	42.4±2.3	153.5±1.8	10749
8612–12702	SDSS J165547.13+391837.8	253.9464	39.3105	SBc	−22.60	8.26	0.0631	52.3±1.0	44.0±1.4	19004

adopted galaxy inclination, and to the fact that these authors used  $H\alpha$  kinematics instead of the stellar velocity fields.

There are some galaxies in our sample that present nuclear activity: 8257–6101 ([Edelson et al. 1987](#); [Toba et al. 2014](#)), 8312–12704 ([Toba et al. 2014](#); [Rembold et al. 2017](#)), 8317–12704 (e.g., [Rembold et al. 2017](#); [Bing et al. 2019](#)), 8320–6101 (e.g., [Stern & Laor 2012](#)), 8326–6102 (e.g., [Greene & Ho 2007](#); [Stern & Laor 2012](#)), 8452–12703 (e.g., [Rembold et al. 2017](#)), 8549–12702 (e.g., [Greene & Ho 2007](#); [Stern & Laor 2012](#)), 8588–3701 (e.g., [Rembold et al. 2017](#)), 8604–12703 (e.g., [Rembold et al. 2017](#)) and 8612–12702

(e.g., [Rembold et al. 2017](#); [Ilha et al. 2019](#)). We did not find any specific peculiarity in the rotation curves of these galaxies, which is to be expected due to the distances involved. Related to this, nuclear activity should not affect the kinematics at large distances from the center (e.g., [Sofue et al. 1999](#); [Schmidt et al. 2016](#); [Sofue 2017](#); [Yu et al. 2022](#)). This would be in accordance with the hypothesis that nuclear activity is generated by a more local cause rather than by a global dynamical mass distribution (e.g., [Sofue et al. 1999](#); [Sofue 2017](#)), although a study with a larger sample size would be necessary to delve deeper into this aspect ([Sánchez et al. 2018b](#)).



**Figure 2.** Distribution of the maximum rotation velocity in units of  $\text{km s}^{-1}$  for our sample of barred galaxies.

On the other hand, as mentioned above, there are galaxies that present evidence of non-circular motions which are manifested through strong departures from the fit. These galaxies are 7962-12703, 7992-6104, 8312-12704, 8317-12704, 8330-12703, 8452-12703, 8482-9102, 8486-6101, 8548-6102 and 8549-12702. This behaviour is expected in this kind of galaxies (e.g., [Vaughan 1989](#); [Regan & Vogel 1994](#); [Schmidt et al. 2019](#)) and may be caused by the presence of nonaxisymmetric structures such as spiral arms and bars (e.g., [Binney et al. 1991](#); [Athanasoula 1992](#); [Burton & Liszt 1993](#); [Sofue 2017](#)).

#### 4.2 Dynamical masses

The derived dynamical masses for all barred galaxies of the sample are presented in column 6 of Table B1. In addition, Fig. 3 shows the distribution of this parameter. The masses are in the range of  $\log(M_{\text{dyn}}/M_{\odot}) = 10.4\text{--}12.0$ , with a mean value of  $\log(M_{\text{dyn}}/M_{\odot}) = 11.1$ . These values are in agreement with previous results considering masses of spiral galaxies (e.g., [Burbidge et al. 1959, 1961](#); [Rubin et al. 1964](#); [Krumm & Salpeter 1977](#); [Pence 1981](#); [Agüero et al. 2004](#); [Salucci et al. 2008](#); [Jalocha et al. 2010](#); [Daod & Zeki 2019](#); [Schmidt et al. 2019](#), among others). The distribution has a standard deviation of 0.36 and an IQR of 0.47. This result would suggest that barred galaxies present dynamical masses similar to those of the general spiral galaxies population.

Considering the uncertainties given by the fitting process of the rotation curves (see Sect. 4.1), the typical relative error in the determination of the dynamical mass is in the range  $\sim 7\% - 15\%$  (Table B1). As mentioned above, these errors take into account only our measurement process.

There are 11 galaxies in our sample which were also studied by [Garma-Oehmichen et al. \(2020\)](#). These objects are 7495-12704, 7962-12703, 8256-6101, 8257-3703, 8312-12704, 8313-9101, 8317-12704, 8318-12703, 8439-6102, 8439-12702 and 8453-12701. These authors present the stellar mass and the molecular gaseous mass derived from the Pipe3D analysis. In the mentioned work, the molec-

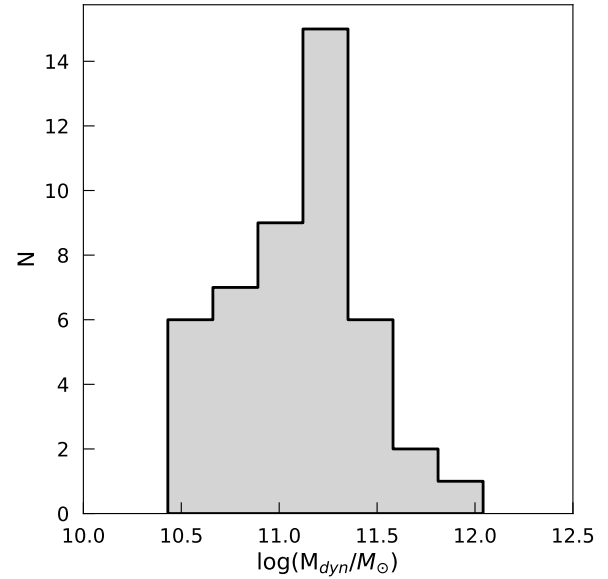


**Figure 3.** Total dynamical mass distribution for our sample of barred galaxies.

ular gas mass was estimated adopting the dust-to-gas ratio based on the dust attenuation obtained by Pipe3D. As expected, the dynamic masses obtained in this work are higher than the sum of the masses obtained in [Garma-Oehmichen et al. \(2020\)](#). This difference is in general  $\sim 0.3$  dex. The observed difference between our dynamically determined mass and the sum of stellar and molecular mass estimates may be attributed to the contribution of other components, such as ionized gas and dark matter (e.g., [Sofue & Rubin 2001](#)). Indeed, it is well-known that the dynamical mass estimates of galaxies account for all gravitationally bound matter within their extent, including components beyond the visible stellar and molecular matter (e.g., [Lelli et al. 2016](#)). In this context, the contribution of ionized gas, which can comprise a substantial fraction of the total gas content in galaxies, can be particularly relevant. Moreover, the presence of dark matter, which is thought to constitute an important fraction of matter in the universe, is expected to impact the dynamical mass of galaxies and, thus, the observed discrepancy between different mass estimates (e.g., [Persic & Salucci 1995](#); [Sofue & Rubin 2001](#); [Lelli et al. 2016](#)). Therefore, our finding of a greater dynamical mass relative to the sum of stellar and molecular mass estimates, while expected, is noteworthy as it underscores the importance of knowing the dynamical masses of these objects as they consider the contribution of all elements to the gravitational potential. To our best knowledge, this is the first direct determination of dynamical masses through rotation curves in this sample of galaxies.

#### 4.3 Stellar masses

The relation between the dynamical and stellar mass of galaxies gives us clues to understand their structure and evolution, since it links the mass already contained in stars with the total mass of the galaxy, i.e. gas, dust, and dark matter. The integrated stellar masses reported in Table B1 were determined from the absorption-corrected stellar mass density maps as indicated in [Sánchez et al. \(2016a,c\)](#). The errors of stellar masses are of the order of  $\sim 1\%$  and were obtained through error propagation considering the mass determination of each spaxel. These errors refer to our measurement process and do not include errors in observations, calibrations, etc. Fig. 4 shows the

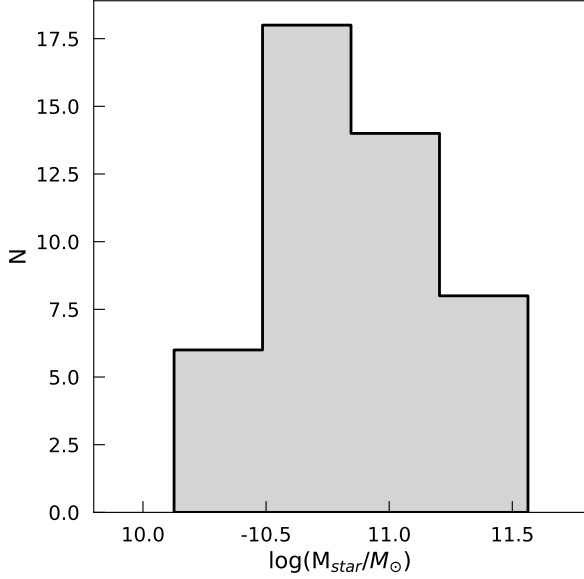


**Figure 4.** Stellar mass distribution for our sample of barred galaxies.

distribution of stellar mass for the whole sample, which is in the range of  $\log(M_{\text{star}}/M_{\odot}) = 10.13 - 11.53$ , with a mean value of  $\log(M_{\text{star}}/M_{\odot}) = 10.8$ . According to our results, this distribution has a standard deviation of 0.35 and an IQR of 0.54. These values are in agreement with previous results on spiral galaxies (e.g., Williams et al. 2010; Davis et al. 2018). As mentioned in Sec.4.2, Garma-Oehmichen et al. (2020) studied the stellar mass of 11 galaxies that are also part of our sample and as expected the results are in good agreement.

#### 4.4 Scaling relations

Scaling relations are empirical relationships between different parameters that can be used to study the properties of galaxies (e.g., Di Teodoro et al. 2021; Krut et al. 2023). They are a fundamental tool for understanding the structure, dynamics, and evolution of galaxies (e.g., Aquino-Ortiz et al. 2018; Ferrero et al. 2021). For example, in the context of rotation curves, scaling relations provide insights into the underlying physical processes that govern the dynamical properties of galaxies. These relations quantify the relationships between different observable properties and are widely used to study the formation and evolution of galaxies (e.g., Lapi et al. 2018; Di Teodoro et al. 2023). As such, scaling relations provide a powerful framework for connecting observations with theoretical models and for testing our understanding of galaxy formation and evolution. In this context, we analyse and study the scaling relations taking into account the magnitude and the parameters we have measured namely dynamical mass, stellar mass, and maximum rotation velocity.

Firstly, we study the relation between the dynamical mass and the stellar mass. In Fig. 5 we show this correlation, which has a Pearson coefficient  $r_p = 0.70$  and a p-value of  $1.4 \times 10^{-7}$ . As expected, this result implies that as the stellar mass of a galaxy increases, so too does its total dynamical mass. Although the relation is clear, it can be seen that there is some dispersion in the data. It is worth noting that there are many different factors that can influence the dynamics of spiral galaxies, including the distribution of dark matter, the presence of gas and dust, and the possible effects of mergers and interactions with

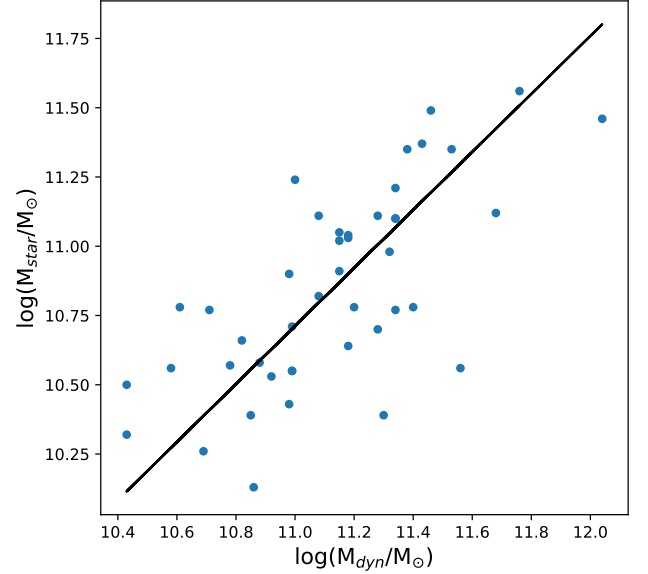


**Figure 5.** Relation between the dynamical mass and the stellar mass. The galaxies 8082-6102 and 8318-12703 are not shown in the plot and are not considered in the analysis. The black solid line represents the OLS bisector fit for our data.

other galaxies. These factors may interact in complex ways and can be different in each galaxy. We performed an OLS (Ordinary Least Squares) bisector fit for our data, which has a slope of  $1.0 \pm 0.1$  and an offset of  $-0.80 \pm 1$ . Due to the deviation, the galaxies 8082–6102 and 8318–12703 are not shown in the plot and are not considered for this particular analysis. These objects, however, are considered for the rest of the analysis regarding the other parameters. Additionally, it has to be noted that a few objects present higher stellar mass compared to the dynamical mass. These galaxies are: 8083-6102, 8249-6101, 8257-3703, 8326-6102, 8548-6104 and 8612-12702 (see Fig. 5 and Table B1). While these differences fall within the errors, caution should be exercised when dealing with these particular values.

In addition, we study the correlation between dynamical mass and maximum rotation velocity, which is a well-known relationship in the study of spiral galaxies (e.g., Rubin et al. 1978). This correlation implies that as the mass of a galaxy increases, so does its maximum rotation velocity. Physically, this can be understood as a result of the balance between gravity and centrifugal forces within the galaxy (e.g., Binney & Tremaine 1987). Fig. 6 shows the relation between the dynamical mass and the maximum rotation velocity. This correlation has a Pearson coefficient  $r_p = 0.90$  and a p-value of  $7.9 \times 10^{-17}$ , indicating the close relationship between the two parameters. As in the previous case, the galaxies 8082–6102 and 8318–12703 are not shown in the plot and are not considered for this particular analysis. These objects, however, are considered for the rest of the analysis. We performed an OLS bisector fit for our data, which has a slope of  $0.33 \pm 0.02$  and an offset of  $-1.36 \pm 0.27$ .

Moreover, in Fig. 7 we show the relation between the stellar mass and the magnitude  $M_r$ . As expected, a close correlation is seen, with a Pearson coefficient  $r_p = -0.93$  and a p-value of  $3.4 \times 10^{-21}$ . The OLS bisector fit has a slope of  $-2.36 \pm 0.12$  and an offset of  $4.2 \pm 1.4$ . As expected, galaxies with higher stellar masses tend to have lower magnitudes, indicating that they are brighter.

In the context of scaling relations, the Tully-Fisher (TF) relation is a powerful tool for understanding the intrinsic properties of rotationally supported galaxies (Tully & Fisher 1977; Courteau 1997a). While

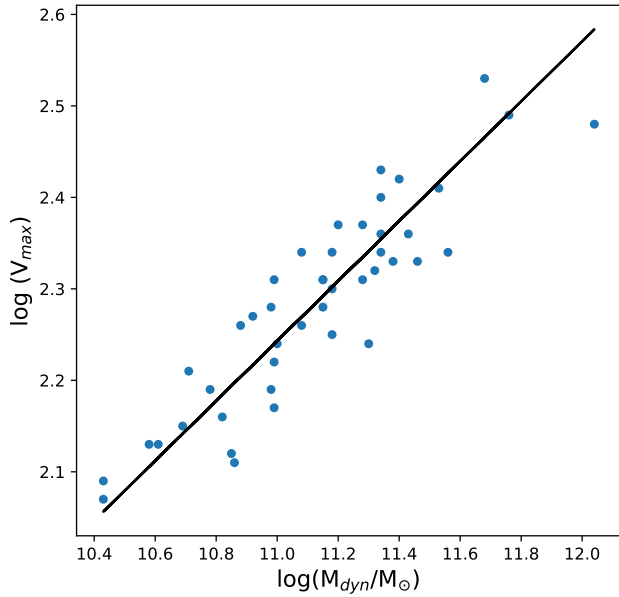


**Figure 6.** Relation between the dynamical mass and the maximum rotation velocity ( $\text{km s}^{-1}$ ). The galaxies 8082-6102 and 8318-12703 are not shown in the plot and are not considered in the analysis. The black solid line represents the OLS bisector fit for our data.

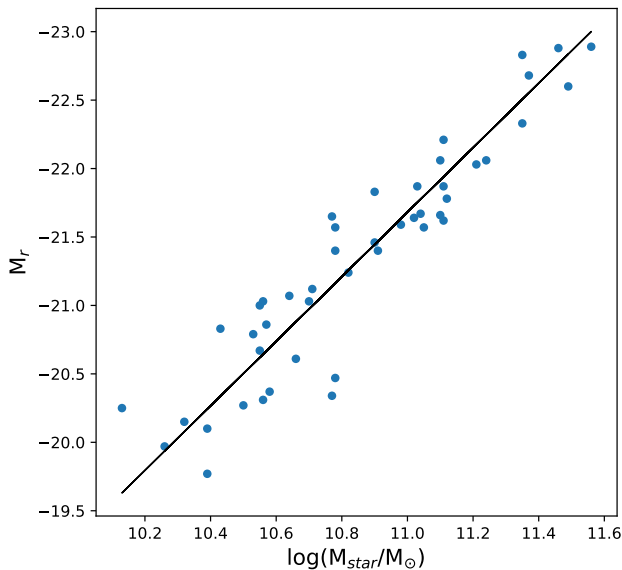


**Figure 7.** Relation between stellar mass and magnitude  $M_r$ . The black solid line represents the OLS bisector fit for our data.

the primary use of the TF relation has been to determine distances in extragalactic studies, it also provides fundamental insights into the mechanisms of disk assembly and evolution (e.g., [Bekeraite 2017](#)). In one of its best-known forms, this relation provides a link between two key properties of galaxies: their circular rotation velocities and their luminosities (e.g., [Pizagno et al. 2007](#); [Bekeraite et al. 2016a](#)). We study the TF relation in our sample through the maximum rotation velocity and the magnitude  $M_r$  (Fig. 8). Considering our data, this relation has a Pearson coefficient  $r_p = -0.76$  and a p-value of  $1.1 \times 10^{-9}$ . An OLS bisector fit yields a slope of  $-7.3 \pm 0.7$  and an offset of  $-4.6 \pm 1.6$ . Our fitting results were compared with [Courteau](#)

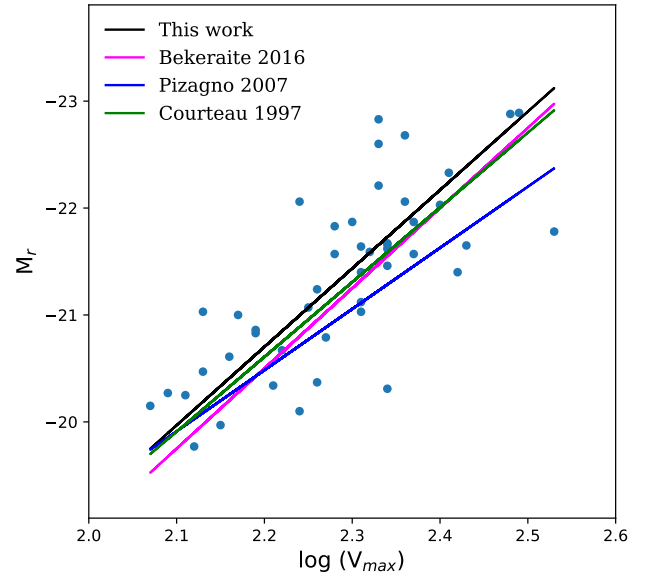


**Figure 8.** T-F relation between the maximum rotation velocity ( $\text{km s}^{-1}$ ) and the magnitude  $M_r$ . The black solid line represents the OLS bisector fit for our data. For comparison we also show the [Courteau \(1997b\)](#), [Pizagno et al. \(2007\)](#) and [Bekeraite et al. \(2016a\)](#) T-F fits.

**Table 2.** Fit parameters of the Tully-Fisher relation ( $V_{max}$  and magnitude  $M_r$ ) and literature values.

Work	Slope	Offset
This work	$-7.3 \pm 0.7$	$-4.6 \pm 1.6$
<a href="#">Bekeraite et al. (2016a)</a>	$-7.5 \pm 0.5$	$-4.0 \pm 1.0$
<a href="#">Pizagno et al. (2007)</a>	$-5.72 \pm 0.19$	$-7.90 \pm 0.03$
<a href="#">Courteau (1997b)</a>	$-6.99 \pm 0.33$	$-5.23 \pm 0.46$

(1997b), [Pizagno et al. \(2007\)](#) and [Bekeraite et al. \(2016a\)](#) findings. The first two studies investigated the TF relation through rotation curves using  $H\alpha$  emission and considering  $\log(v)$  as independent variable. On the other hand, [Bekeraite et al. \(2016a\)](#) explored the TF relation in a sample of galaxies from CALIFA using stellar dynamics and considering the magnitude as the independent variable. Our bisector fit's slope and offset are presented in Table 2, along with the corresponding values reported by [Courteau \(1997b\)](#), [Pizagno et al. \(2007\)](#) and [Bekeraite et al. \(2016a\)](#) (see Table 1 of this last work). As can be seen, the slope and offset reported in this work are within the range obtained by [Bekeraite et al. \(2016a\)](#) and [Courteau \(1997b\)](#). This suggests that the behaviour of the sample of barred galaxies considering this relation does not differ from that of other studies involving galaxies of different morphological types including non-barred galaxies.

A known alternative form of the TF relation is expressed in terms of the stellar mass and the maximum rotation velocity (e.g., [Avila-Reese et al. 2008](#)). We examine this relation in Fig. 9, which has a Pearson coefficient  $r_p = 0.74$  and a p-value of  $3.3 \times 10^{-9}$ . The OLS bisector fit has a slope of  $0.32 \pm 0.03$  and an offset of  $-1.2 \pm 0.3$ . We compared our fitting results with those found by [Avila-Reese et al. \(2008\)](#) and [Aquino-Ortiz et al. \(2018\)](#). [Avila-Reese et al. \(2008\)](#) study the TF relation in a compiled sample of 76 normal disk galaxies of all morphological types and performed, among others, a bisector fit (their table 1), while [Aquino-Ortiz et al. \(2018\)](#) study



**Table 3.** Fit parameters of the Tully-Fisher relation ( $M_{\text{star}}/M_{\odot}$  and  $V_{\text{max}}$  in  $\text{km s}^{-1}$ ) and literature values.

Work	Slope	Offset
This work	$0.32 \pm 0.03$	$-1.2 \pm 0.3$
Aquino-Ortíz et al. (2018)	$0.30 \pm 0.02$	$-1.00 \pm 0.02$
Avila-Reese et al. (2008)	$0.284 \pm 0.012$	$-0.741 \pm 0.127$

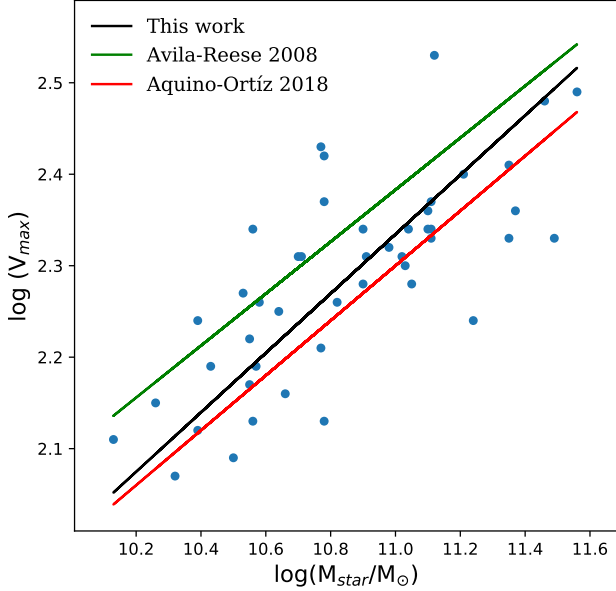


**Figure 9.** T-F relation between the stellar mass and the maximum rotation velocity ( $\text{km s}^{-1}$ ). The black solid line represents the OLS bisector fit for our data. For comparison we also show the Aquino-Ortíz et al. (2018) and Avila-Reese et al. (2008) T-F fits.

the TF relation in galaxies from CALIFA performing an orthogonal linear fit considering, among others, the stellar dynamics of only spiral galaxies and using the stellar mass as independent variable (their table 1). In Table 3 we present our values of slope and offset for our bisector fit of the TF relation. This table also shows the parameters provided by Avila-Reese et al. (2008) and Aquino-Ortíz et al. (2018). The slope value we obtain is higher than the values obtained by both works, however, within error it is similar to the one reported by Aquino-Ortíz et al. (2018). In Fig. 9 it can be seen that our fit is between the fits of these two mentioned works, what indicates that the behaviour of this sample of barred galaxies does not differ from samples of varying morphologies.

## 5 COMPARISON WITH LITERATURE

This section presents a comparison of the parameters obtained for our sample of galaxies with those of other samples found in the literature. The primary objective is to examine the results in relation to other studies on barred galaxies and to investigate potential differences between barred and non-barred galaxies in terms of their stellar mass, total mass, and  $V_{\text{rot}}$ . By conducting this analysis, we aim to gain a deeper understanding of the properties and behavior of barred galaxies and how they relate to the broader population of galaxies.

We compared the stellar mass distribution of our sample with

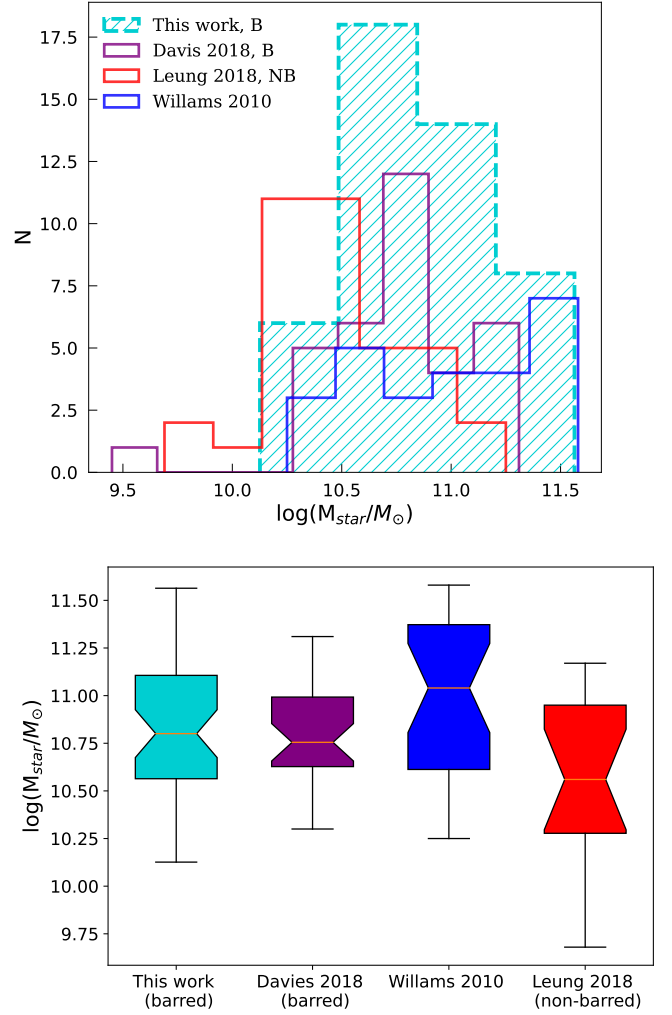


**Figure 10.** Comparison of distributions of stellar mass for our sample and other three spiral galaxy samples (see text for details). Top panel shows histograms for each sample with the barred and non-barred samples marked with "B" and "NB" labels. The bottom panel displays box plots with the same color scheme. The orange horizontal line within each box plot represents the median value. The height of the boxes indicate the interquartile range (IQR) for each sample, while the whiskers extending from the boxes indicate the range of non-outlier values. Additionally, the notches in the boxes provide a visual estimate of the statistical significance of differences between groups. If the notches of two boxes do not overlap, it suggests that there is a significant difference in the medians of the two groups at a 95% confidence level.

three additional samples of spiral galaxies by generating histograms and box plots (see Fig. 10). Box plots are an effective tool for summarising the distribution of data based on quartiles and offer several advantages, including the ability to visualize central tendency, dispersion, and outliers of each sample, even for small samples ( $n > 5$ ). In addition, we have included the histograms of the samples as they provide a quick and direct visualization of their distributions. Barred and non-barred galaxies were distinguished for each sample using the morphological type reported in the NED, and we only included in this analysis sub-samples with a sufficient number of galaxies to conduct a meaningful comparison.

Of the sub-samples examined, only the sample presented in Davis

et al. (2018) contained a sufficient number of barred galaxies for a valid comparison. The medians of our sample and the Davis et al. (2018) sample are statistically similar, as shown in the bottom panel of Fig. 10, taking into account the uncertainties represented by the notches of the boxes. Furthermore, we used the Kolmogorov-Smirnov (KS) test to compare the underlying distributions of the two samples and obtained a statistic of 0.2123 and a p-value of 0.2895. As the p-value is significantly higher than the limit value of 0.05, there is no strong evidence to reject the null hypothesis. Therefore, based on the KS test, it is likely that the two samples were drawn from the same underlying distribution suggesting that our sample and the sample of Davis et al. (2018) may follow a similar stellar mass distribution.

The non-barred sub-sample we used to compare our results came from Leung et al. (2018) where the stellar masses were measured for the EDGE-CALIFA survey (Bolatto et al. 2017), which mainly includes face-on galaxies. The box plot in Fig. 10 reveals some overlapping between our sample and the sample from Leung et al. (2018) but the medians of both samples are clearly different. The KS test yielded a statistic of 0.3849 and a p-value of 0.0008 for the comparison between them, indicating that the two samples likely have different underlying distributions. This suggests that there could be a statistically significant difference in the stellar mass distributions of barred and non-barred galaxies.

Finally, we compared our stellar masses with a third sample of edge-on spiral galaxies compiled by Williams et al. (2010). We have selected only the non-barred galaxies based on their classification in the NED. However, we note that despite the NED classification, Williams et al. (2010) report that 75% of the galaxies in this sample exhibit boxy structures that may be interpreted as bars viewed side-on. Furthermore, given that all galaxies in this sample are edge-on and that bars in such galaxies may be harder to observe, it is likely that this sample is strongly contaminated with barred galaxies. As such, care must be taken when comparing our results to this sample. The box plot in Fig. 10 shows a significant difference between the median of the stellar mass for this sample and ours and even more with respect to the non-barred sample from Leung et al. (2018). For the comparison with our sample the KS test yielded similar results as the obtained when comparing with the barred sample of Davis et al. (2018): a statistic of 0.2876 and a p-value=0.1016, implicating that we can not rule out the null hypothesis where both samples, ours and the one from Williams et al. (2010), have been drawn from the same stellar mass distribution. This reinforces the idea that the galaxies in Williams et al. (2010) sample could be mainly barred.

Regarding the total dynamical mass we found that Williams et al. (2010) used the  $K_s$  total magnitude to estimate the total mass of the galaxies in their sample. To evaluate the agreement between their result and our own, we present a comparison in Fig. 11, where we used histograms and box plots to illustrate the distributions of both samples. Despite the relatively small sample size in Williams et al. (2010), our analysis indicates significant agreement between the two datasets. Results from a KS test yield a statistic of 0.1572 and a corresponding p-value of 0.7364, indicating that the two distributions are statistically indistinguishable within the limits of these samples.

In order to compare the  $V_{max}$  values of our sample with those of other studies, we used a sample of spiral galaxies presented by Rubin et al. (1980). We employed the NED to classify the galaxies into barred and non-barred subsamples, which resulted in 12 and 9 galaxies, respectively. Although the sample size is relatively low, we conducted a statistical analysis to investigate the differences between the samples. The histograms and box-plots depicted in Fig. 12 suggest that the three samples are statistically indistinguishable.

Furthermore, we implemented the Kolmogorov-Smirnov test to

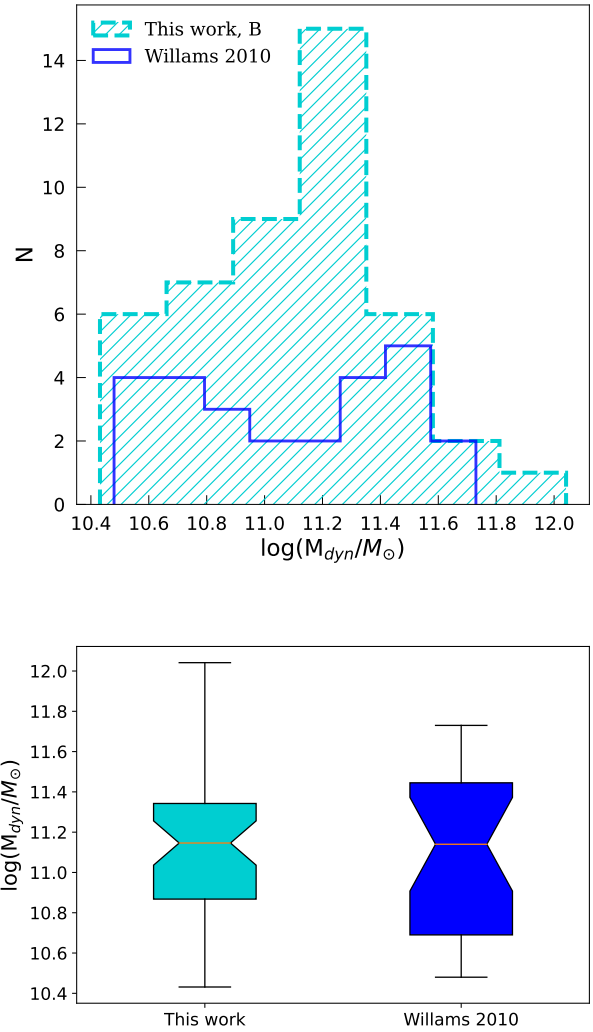
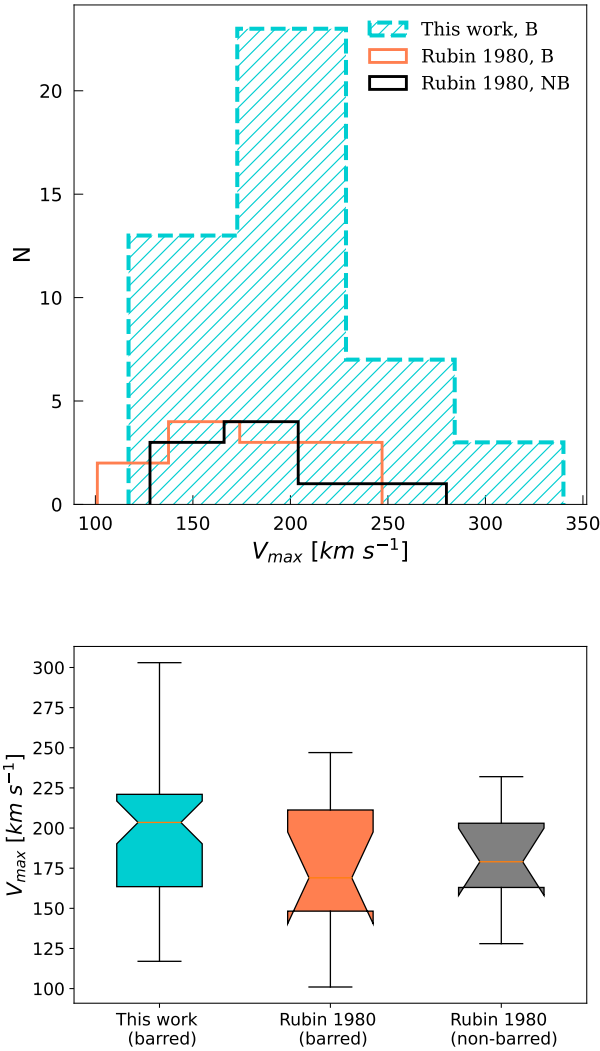


Figure 11. Same as Fig. 10 but for the total dynamical mass.

evaluate the significance of the similarities and differences between the samples. The test yielded a statistic of 0.2608 and a p-value of 0.4612 for the comparison between our sample and the barred sample of Rubin et al. (1980). Additionally, we obtained a statistic of 0.2777 and a p-value of 0.5121 for the comparison with their non-barred sample. In both cases, the null hypothesis of the samples corresponding to the same distribution cannot be rejected. Thus, based on the KS test, we can conclude that the two samples are statistically similar to ours in their distribution, even though caution should be exercised due to the low number of galaxies in each of the sub-samples from Rubin et al. (1980). A larger sample of non-barred galaxies is necessary in order to study if bars have some impact in the  $V_{max}$  of galaxies.

## 6 FINAL REMARKS

We have obtained and presented the rotation curves of 46 barred galaxies of MaNGA (Fig. A1). By intrinsic quality of the individual curves, size, and homogeneity, this sample constitutes one of the



**Figure 12.** Same as Fig. 10 but for the maximum velocity.

best samples of RCs available for barred galaxies to date. As such, it will offer a very good opportunity for investigating and analyzing the dynamical properties of this kind of objects.

We have fitted all the RCs considering two components of an axisymmetric Miyamoto–Nagai gravitational potential, the parameters of which are presented in Table B1. Our main results can be summarised as follows:

- We have found a wide range of rotation velocities ( $117 - 340 \text{ km s}^{-1}$ ), with most galaxies showing values in the range  $120 - 250 \text{ km s}^{-1}$ . These velocities are consistent with previous results in barred galaxies and no difference have been found with a sample of non-barred galaxies. Nevertheless a larger sample of galaxies is necessary to confirm this trend.

- The total dynamical masses of our sample lie in the range of  $\log(M_{\text{dyn}}/M_{\odot}) = 10.1 - 12.0$ , with a mean value of  $\log(M_{\text{dyn}}/M_{\odot}) = 11.0$ . These values are in agreement with previous results considering total masses of spiral galaxies. According to our results, the distribution has a standard deviation of 0.39 and an IQR of 0.55.

- Stellar masses of our sample of barred galaxies are in the range  $\log(M_{\text{star}}/M_{\odot}) = 10.13 - 11.53$  with a standard deviation of 0.35 and an IQR of 0.54. The comparison with other sample of barred galaxies yielded no statistical difference while comparison with a non-barred galaxies sample yielded that both distributions are statistically different. This difference between the stellar mass of barred and non-barred galaxies could imply that the bar plays a role in the assembly of stellar mass of galaxies.

- The behaviour of our sample in the scaling relations was investigated. We found a Pearson coefficient  $r_p = 0.70$  and a p-value of  $1.4 \times 10^{-7}$  for the relation between  $M_{\text{dyn}}$  and  $M_{\text{star}}$  while for the relation between  $M_{\text{dyn}}$  and  $V_{\text{max}}$  the statistic yielded  $r_p = 0.9$  and a p-value of  $7.9 \times 10^{-17}$ . We also explored the Tully-Fisher relation in two ways: by considering the relationship between  $V_{\text{max}}$  and  $M_r$  ( $r_p = -0.76$  and a p-value of  $1.1 \times 10^{-9}$ ), and separately by examining  $V_{\text{max}}$  and  $M_{\text{star}}$  ( $r_p = 0.74$  and a p-value of  $3.3 \times 10^{-9}$ ). Our analysis revealed that the Tully-Fisher relation in barred galaxies is consistent with reported relations in the literature for samples of varying morphologies, indicating that barred galaxies do not deviate from this scaling relation commonly observed in other galaxy types.

Summing up, we studied the dynamical masses, stellar masses and maximum rotation velocities of barred galaxies, investigating their distributions and scaling relations and comparing them with other studies. Our results suggest that stellar masses could be different in barred galaxies compared with non-barred galaxies. The dynamical mass and maximum rotation velocities as well as scaling relations such as the Tully-Fisher relation show no difference with other samples involving galaxies with different morphological types including non-barred galaxies.

It has to be noted the importance of knowing the dynamical masses of galaxies as they consider the contribution of all constituent elements to the gravitational potential. To our best knowledge, this is the first time that the dynamical masses of these galaxies have been determined in a direct and independent way through their rotation curves. We hope that the work presented here will constitute a useful tool to increase our understanding of the dynamical behaviour of barred spiral galaxies.

## ACKNOWLEDGEMENTS

We want to thank our referee for constructive comments and suggestions that improved this work. We are also grateful to Rubén Díaz for fruitful discussions. This work was partially supported by grant PICT 2017-3301 awarded by Fondo para la Investigación Científica y Tecnológica (FonCyT). G.G is a postdoctoral fellow of Consejo de Investigaciones Científicas y Técnicas (CONICET), Argentina. W.W., E.S., and D.M. are members of the Carrera del Investigador Científico of CONICET, Argentina. This research has made use of the NASA/IPAC Extragalactic Database (NED) which is operated by the Jet Propulsion Laboratory, California Institute of Technology, under contract with the National Aeronautics and Space Administration. We made an extensive use of the following Python libraries and packages: *galpy*, *pandas*, *Matplotlib*, *NumPy* and *SciPy*. This project makes use of the MaNGA-Pipe3D dataproducs. We thank the IA-UNAM MaNGA team for creating this catalogue, and the ConaCyt-180125 project for supporting them. Funding for the Sloan Digital Sky Survey IV has been provided by the Alfred P. Sloan Foundation, the U.S. Department of Energy Office of Science, and the Participating Institutions. SDSS acknowledges support and re-

sources from the Center for High-Performance Computing at the University of Utah. The SDSS web site is [www.sdss.org](http://www.sdss.org). SDSS is managed by the Astrophysical Research Consortium for the Participating Institutions of the SDSS Collaboration including the Brazilian Participation Group, the Carnegie Institution for Science, Carnegie Mellon University, Center for Astrophysics | Harvard & Smithsonian (CfA), the Chilean Participation Group, the French Participation Group, Instituto de Astrofísica de Canarias, The Johns Hopkins University, Kavli Institute for the Physics and Mathematics of the Universe (IPMU) / University of Tokyo, the Korean Participation Group, Lawrence Berkeley National Laboratory, Leibniz Institut für Astrophysik Potsdam (AIP), Max-Planck-Institut für Astronomie (MPIA Heidelberg), Max-Planck-Institut für Astrophysik (MPA Garching), Max-Planck-Institut für Extraterrestrische Physik (MPE), National Astronomical Observatories of China, New Mexico State University, New York University, University of Notre Dame, Observatório Nacional / MCTI, The Ohio State University, Pennsylvania State University, Shanghai Astronomical Observatory, United Kingdom Participation Group, Universidad Nacional Autónoma de México, University of Arizona, University of Colorado Boulder, University of Oxford, University of Portsmouth, University of Utah, University of Virginia, University of Washington, University of Wisconsin, Vanderbilt University, and Yale University.

## DATA AVAILABILITY

All data used and analysed in this article are available in [www.sdss.org/dr17/](http://www.sdss.org/dr17/)

## REFERENCES

- Adams J. J., Gebhardt K., Blanc G. A., Fabricius M. H., Hill G. J., Murphy J. D., van den Bosch R. C. E., van de Ven G., 2012, *ApJ*, **745**, 92
- Agüero E. L., Díaz R. J., Bajaja E., 2004, *A&A*, **414**, 453
- Aguerri J. A. L., Méndez-Abreu J., Corsini E. M., 2009, *A&A*, **495**, 491
- Ahn C. P., et al., 2012, *ApJS*, **203**, 21
- Albareti F. D., et al., 2017, *ApJS*, **233**, 25
- Aquino-Ortíz E., et al., 2018, *MNRAS*, **479**, 2133
- Aquino-Ortíz E., et al., 2020, *ApJ*, **900**, 109
- Ashman K. M., 1992, *PASP*, **104**, 1109
- Athanassoula E., 1992, *MNRAS*, **259**, 328
- Avila-Reese V., Zavala J., Firmani C., Hernández-Toledo H. M., 2008, *AJ*, **136**, 1340
- Barrera-Ballesteros J. K., et al., 2014, *A&A*, **568**, A70
- Bekeraite S., 2017, PhD thesis, University of Potsdam, Germany
- Bekeraite S., et al., 2016a, *A&A*, **593**, A114
- Bekeraite S., et al., 2016b, *ApJ*, **827**, L36
- Bing L., et al., 2019, *MNRAS*, **482**, 194
- Binney J., Tremaine S., 1987, *Galactic dynamics*
- Binney J., Gerhard O. E., Stark A. A., Bally J., Uchida K. I., 1991, *MNRAS*, **252**, 210
- Bolatto A. D., et al., 2017, *ApJ*, **846**, 159
- Bosma A., 1996, in Buta R., Crocker D. A., Elmegreen B. G., eds, *Astronomical Society of the Pacific Conference Series Vol. 91, IAU Colloq. 157: Barred Galaxies*, p. 132
- Bovy J., 2015, *ApJS*, **216**, 29
- Bundy K., et al., 2015, *ApJ*, **798**, 7
- Burbidge E. M., Burbidge G. R., Prendergast K. H., 1959, *ApJ*, **130**, 739
- Burbidge E. M., Burbidge G. R., Prendergast K. H., 1961, *ApJ*, **134**, 874
- Bureau M., Carignan C., 2002, *AJ*, **123**, 1316
- Burton W. B., Liszt H. S., 1993, *A&A*, **274**, 765
- Cappellari M., 2017, *MNRAS*, **466**, 798
- Cappellari M., Emsellem E., 2004, *PASP*, **116**, 138
- Cherinka B., et al., 2019, *AJ*, **158**, 74
- Ciotti L., 2021, *Introduction to Stellar Dynamics*, doi:10.1017/9780511736117.
- Ciotti L., 2022, *ApJ*, **936**, 180
- Courteau S., 1997a, *AJ*, **114**, 2402
- Courteau S., 1997b, *AJ*, **114**, 2402
- Croom S. M., et al., 2012, *MNRAS*, **421**, 872
- Daod N. A., Zeki M. K., 2019, *ApJ*, **870**, 107
- Davis B. L., Graham A. W., Cameron E., 2018, *ApJ*, **869**, 113
- Di Teodoro E. M., Posti L., Ogle P. M., Fall S. M., Jarrett T., 2021, *MNRAS*, **507**, 5820
- Di Teodoro E. M., et al., 2023, *MNRAS*, **518**, 6340
- Díaz R., Carranza G., Dottori H., Goldes G., 1999, *ApJ*, **512**, 623
- Edelson R. A., Malkan M. A., Rieke G. H., 1987, *ApJ*, **321**, 233
- Falcón-Barroso J., et al., 2017, *A&A*, **597**, A48
- Ferrero I., Navarro J. F., Abadi M. G., Benavides J. A., Mast D., 2021, *A&A*, **648**, A124
- García-Lorenzo B., et al., 2015, *A&A*, **573**, A59
- Garma-Oehmichen L., Cano-Díaz M., Hernández-Toledo H., Aquino-Ortíz E., Valenzuela O., Aguerri J. A. L., Sánchez S. F., Merrifield M., 2020, *MNRAS*, **491**, 3655
- Granados A., Torres D., Castañeda L., Henao-O. J. L., Vanegas S., 2017, arXiv e-prints, p. arXiv:1705.01665
- Greene J. E., Ho L. C., 2007, *ApJ*, **667**, 131
- Gunn J. E., et al., 2006, *AJ*, **131**, 2332
- Guo R., Mao S., Athanassoula E., Li H., Ge J., Long R. J., Merrifield M., Masters K., 2019, *MNRAS*, **482**, 1733
- Hernandez O., Carignan C., Amram P., Chemin L., Daigle O., 2005, *MNRAS*, **360**, 1201
- Ilha G. S., et al., 2019, *MNRAS*, **484**, 252
- Jałocha J., Bratek Ł., Kutschera M., Skindzier P., 2010, *MNRAS*, **406**, 2805
- Kalinova V., van de Ven G., Lyubenova M., Falcón-Barroso J., Colombo D., Rosolowsky E., 2017a, *MNRAS*, **464**, 1903
- Kalinova V., et al., 2017b, *MNRAS*, **469**, 2539
- Krumm N., Salpeter E. E., 1977, *A&A*, **56**, 465
- Krut A., Argüelles C. R., Chavanis P. H., Rueda J. A., Ruffini R., 2023, *ApJ*, **945**, 1
- Laine S., Kenney J. D. P., Yun M. S., Gottesman S. T., 1999, *ApJ*, **511**, 709
- Lang P., et al., 2020, *ApJ*, **897**, 122
- Lapi A., Salucci P., Danese L., 2018, *ApJ*, **859**, 2
- Lelli F., McGaugh S. S., Schombert J. M., Pawłowski M. S., 2016, *ApJ*, **827**, L19
- Leung G. Y. C., et al., 2018, *MNRAS*, **477**, 254
- Levy R. C., et al., 2018, *ApJ*, **860**, 92
- Makarov D. I., Burenkov A. N., Tyurina N. V., 2001, *Astronomy Letters*, **27**, 213
- Marinova I., Jogee S., 2007, *ApJ*, **659**, 1176
- Márquez I., Masegosa J., Moles M., Varela J., Bettoni D., Galletta G., 2002, *A&A*, **393**, 389
- Martínez-Medina L. A., Pichardo B., Peimbert A., 2020, *MNRAS*, **496**, 1845
- Martinsson T. P. K., Verheijen M. A. W., Westfall K. B., Bershadsky M. A., Schechtman-Rook A., Andersen D. R., Swaters R. A., 2013, *A&A*, **557**, A130
- Mathewson D. S., Ford V. L., Buchhorn M., 1992, *ApJS*, **81**, 413
- Miyamoto M., Nagai R., 1975, *Publications of the Astronomical Society of Japan*, **27**, 533
- Pence W. D., 1981, *ApJ*, **247**, 473
- Persic M., Salucci P., 1995, *ApJS*, **99**, 501
- Pilyugin L. S., Grebel E. K., Zinchenko I. A., Nefedyev Y. A., Vilchez J. M., 2019, *A&A*, **623**, A122
- Pizagno J., et al., 2007, *AJ*, **134**, 945
- Regan M. W., Vogel S. N., 1994, *ApJ*, **434**, 536
- Rembold S. B., et al., 2017, *MNRAS*, **472**, 4382
- Rubin V. C., Burbidge E. M., Burbidge G. R., Prendergast K. H., 1964, *ApJ*, **140**, 80
- Rubin V. C., Ford W. K. J., Thonnard N., 1978, *ApJ*, **225**, L107
- Rubin V. C., Ford W. K. J., Thonnard N., 1980, *ApJ*, **238**, 471
- Salucci P., Yegorova I. A., Drory N., 2008, *MNRAS*, **388**, 159



- Sánchez S. F., et al., 2012, [A&A](#), **538**, A8
- Sánchez S. F., et al., 2016a, *Rev. Mex. Astron. Astrofis.*, **52**, 21
- Sánchez S. F., et al., 2016b, *Rev. Mex. Astron. Astrofis.*, **52**, 171
- Sánchez S. F., et al., 2016c, *Rev. Mex. Astron. Astrofis.*, **52**, 171
- Sánchez S. F., et al., 2018a, *Rev. Mex. Astron. Astrofis.*, **54**, 217
- Sánchez S. F., et al., 2018b, *Rev. Mex. Astron. Astrofis.*, **54**, 217
- Schmidt E. O., Ferreira D., Vega Neme L., Oio G. A., 2016, [A&A](#), **596**, A95
- Schmidt E. O., Mast D., Díaz R. J., Agüero M. P., Günthardt G., Gimeno G., Oio G., Gaspar G., 2019, [AJ](#), **158**, 60
- Sheth K., et al., 2008, [ApJ](#), **675**, 1141
- Shetty R., Vogel S. N., Ostriker E. C., Teuben P. J., 2007, [ApJ](#), **665**, 1138
- Sofue Y., 2016, [PASJ](#), **68**, 2
- Sofue Y., 2017, [PASJ](#), **69**, R1
- Sofue Y., Rubin V., 2001, [ARA&A](#), **39**, 137
- Sofue Y., Tutui Y., Honma M., Tomita A., Takamiya T., Koda J., Takeda Y., 1999, [ApJ](#), **523**, 136
- Spano M., Marcellin M., Amram P., Carignan C., Epinat B., Hernandez O., 2008, [MNRAS](#), **383**, 297
- Stern J., Laor A., 2012, [MNRAS](#), **423**, 600
- Toba Y., et al., 2014, [ApJ](#), **788**, 45
- Tully R. B., Fisher J. R., 1977, [A&A](#), **54**, 661
- Vaughan J. M., 1989, *The Fabry-Perot interferometer. History, theory, practice and applications*
- Vogt N. P., Haynes M. P., Giovanelli R., Herter T., 2004a, [AJ](#), **127**, 3300
- Vogt N. P., Haynes M. P., Giovanelli R., Herter T., 2004b, [AJ](#), **127**, 3325
- Williams M. J., Bureau M., Cappellari M., 2010, [MNRAS](#), **409**, 1330
- Yoon Y., Park C., Chung H., Zhang K., 2021, [ApJ](#), **922**, 249
- Yu S.-Y., et al., 2022, [A&A](#), **666**, A175

## APPENDIX A: FITTED ROTATION CURVES OF THE 46 BARRED GALAXIES

## APPENDIX B: DYNAMICAL PARAMETERS OF THE GALAXIES

This paper has been typeset from a  $\text{\LaTeX}$  file prepared by the author.

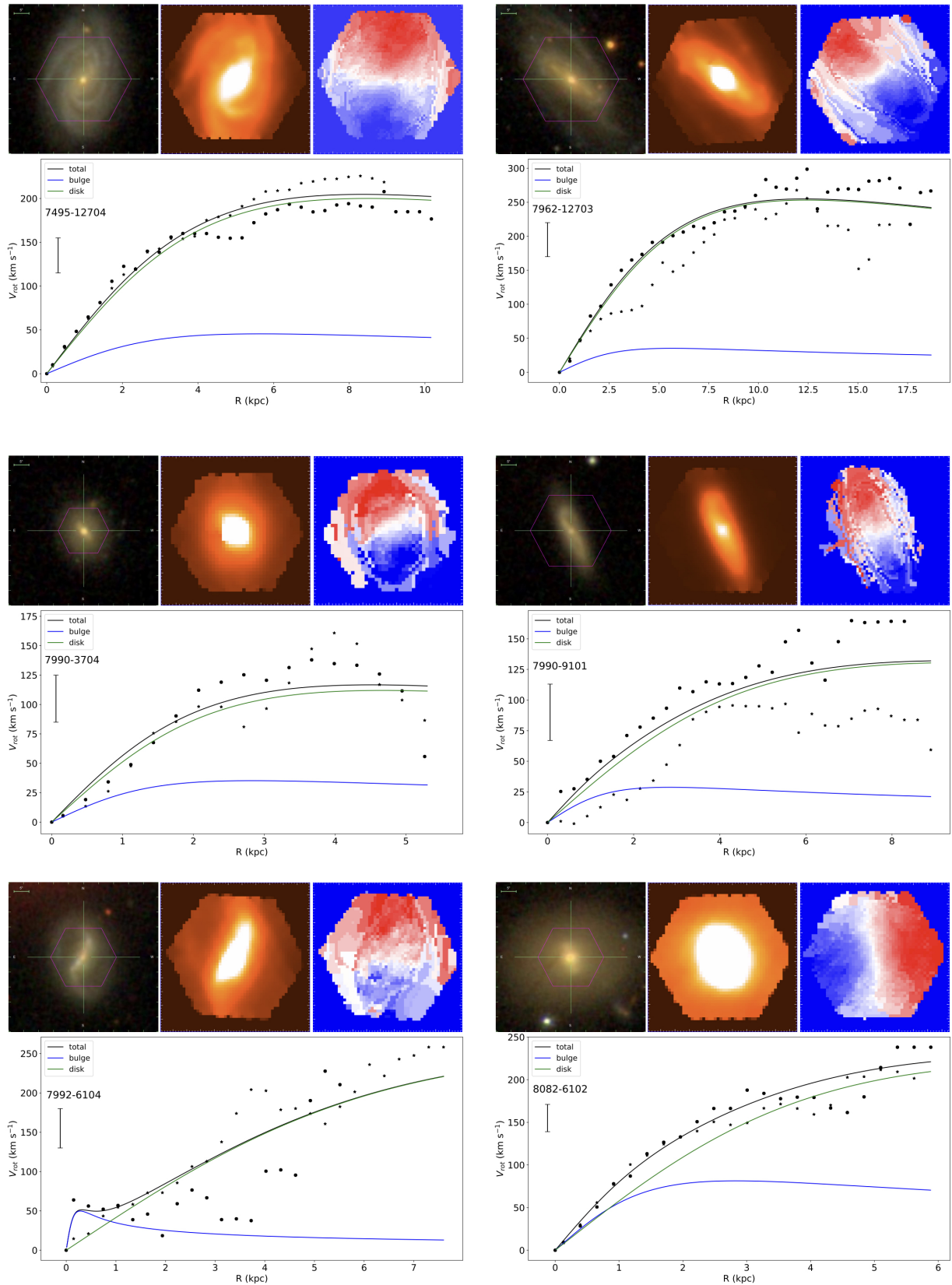


**Figure A1.** Each panel shows from left to right and top to bottom: MaNGA FoV depicted over *gri* false-color images from SDSS, pseudo-V-band image extracted from the datacubes, the velocity field with red color representing positive radial velocities and blue representing negative radial velocities with respect to the systemic velocity (see text for details), and the rotation curve fitted with two mass components corresponding to an axisymmetric Miyamoto–Nagai gravitational potential. In all the maps and images, North is up and East is to the left. Note that the maps are not at the same scale as the false color image. Tickmarks on the maps are separated each 0.5 arcsec. Circles and stars represent different sides of the velocity field. A typical error bar is shown in the top left corner.

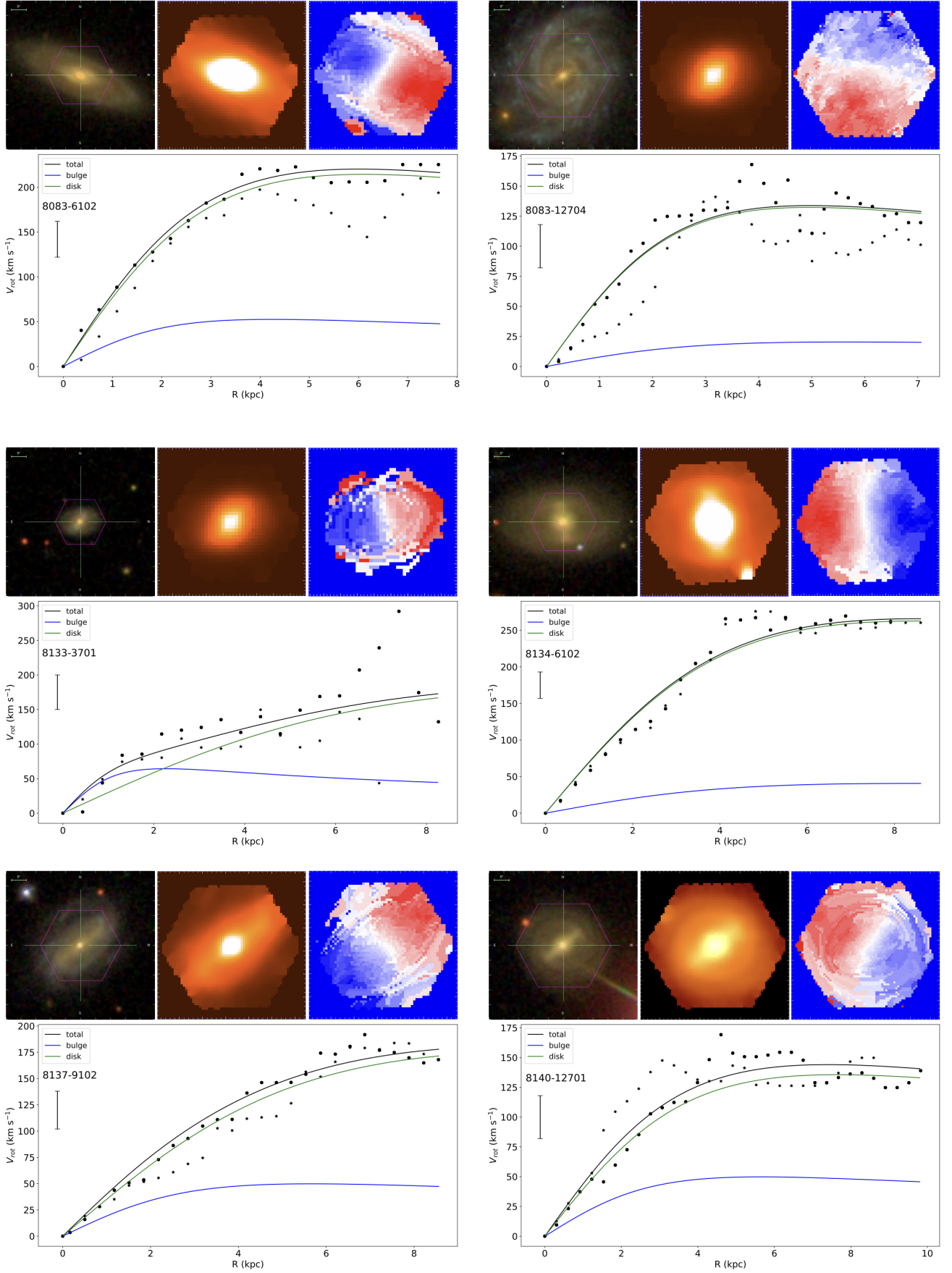


Figure A1. continued

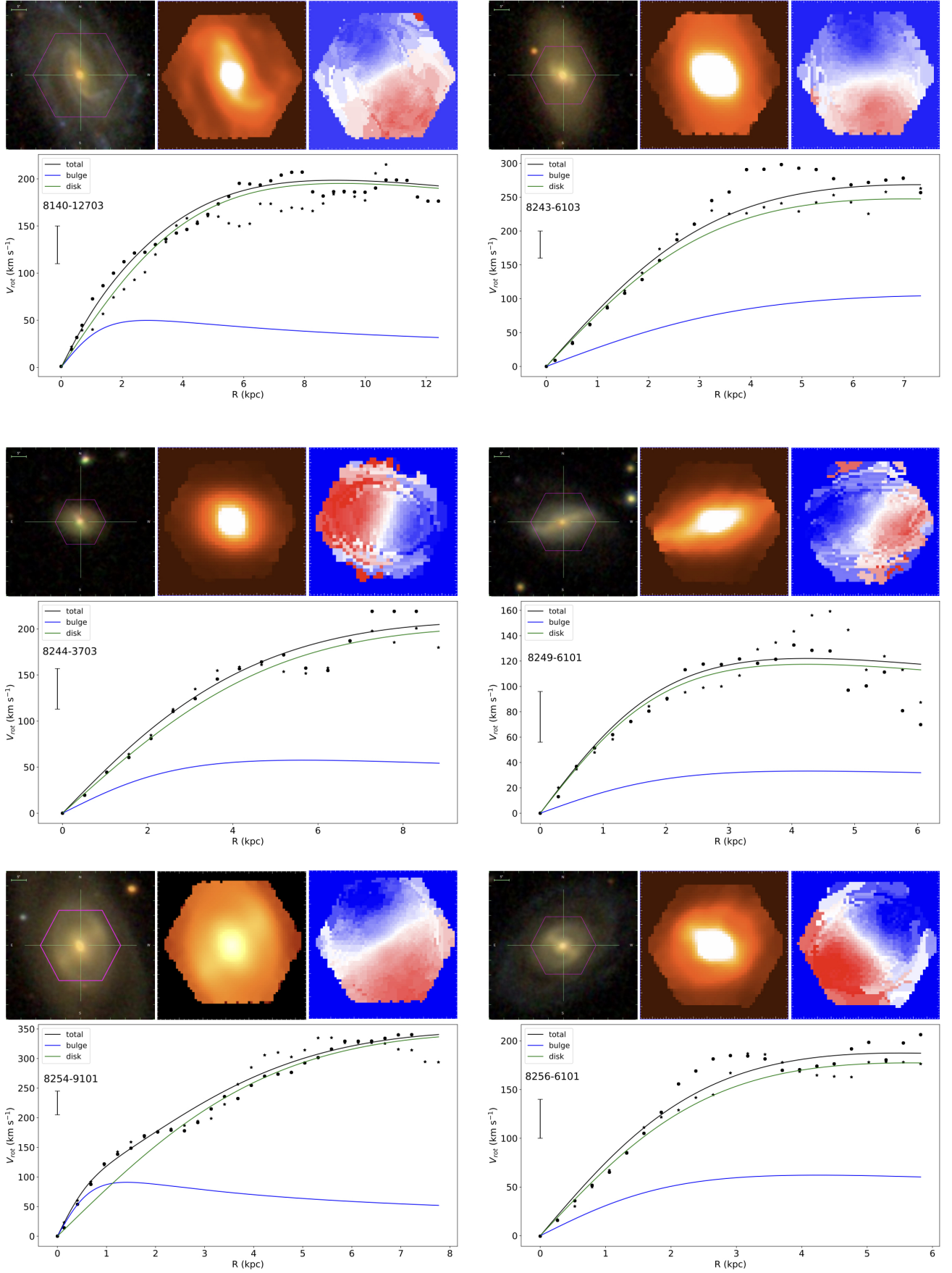


Figure A1. continued



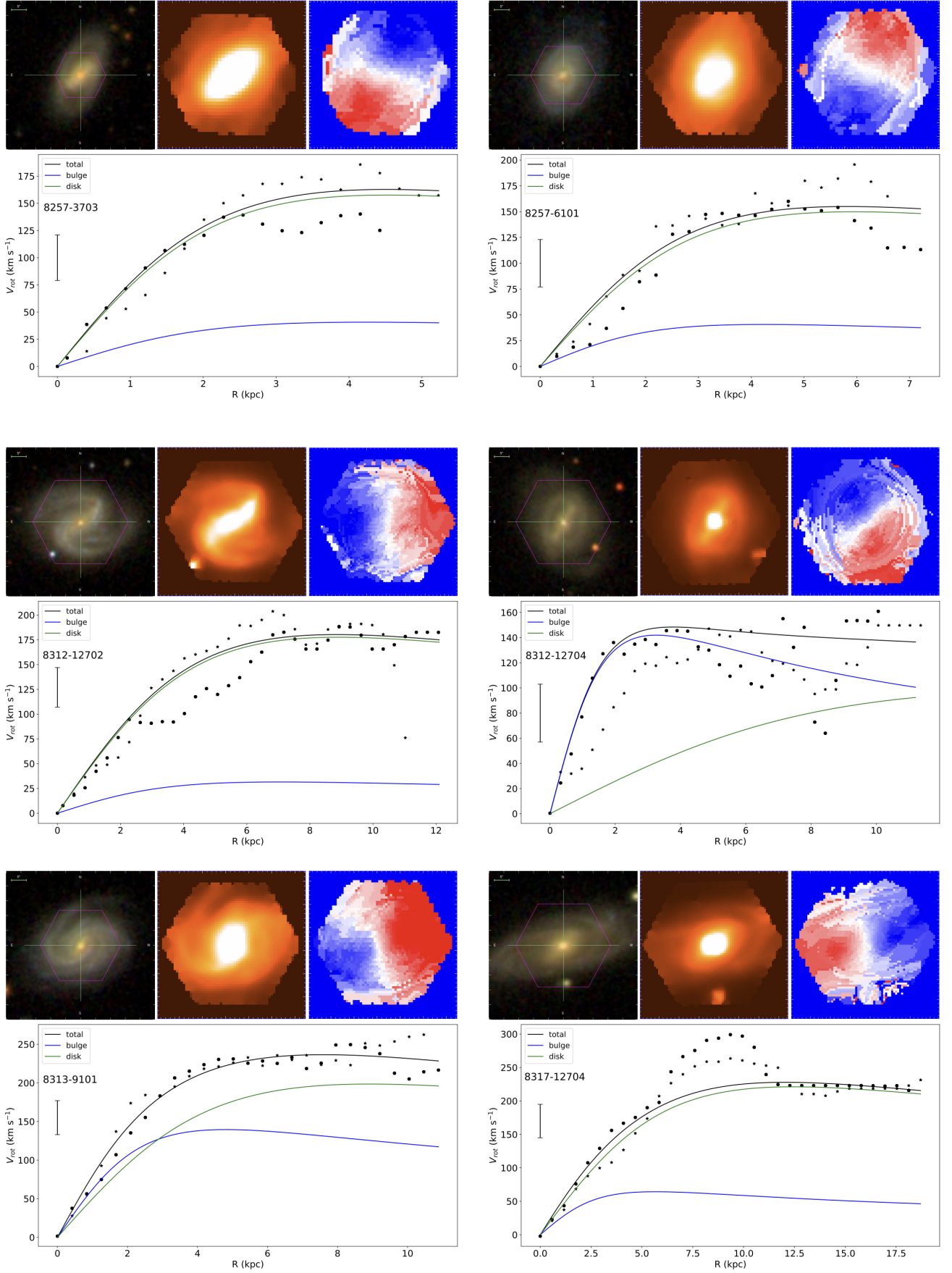


Figure A1. continued

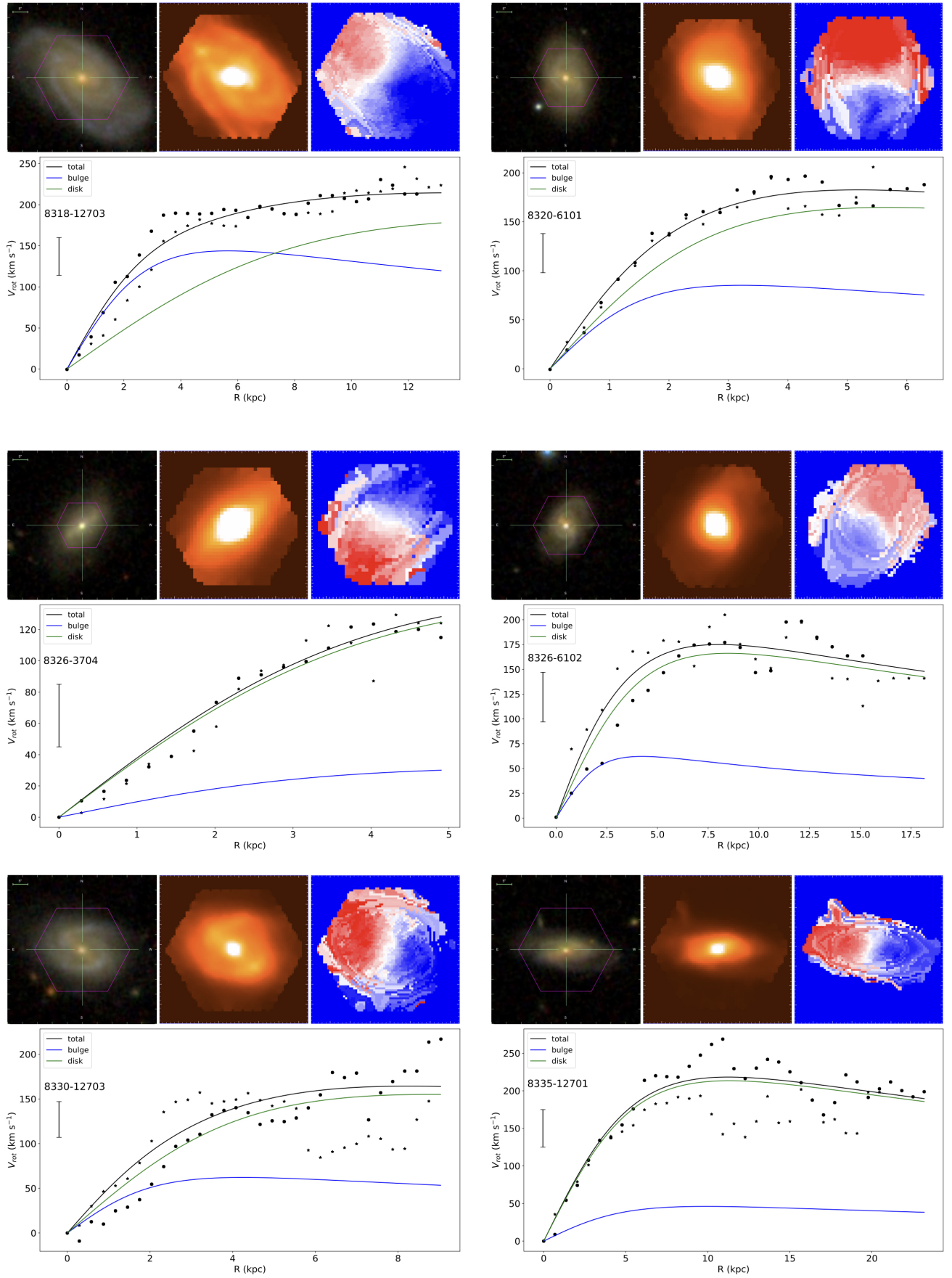


Figure A1. continued

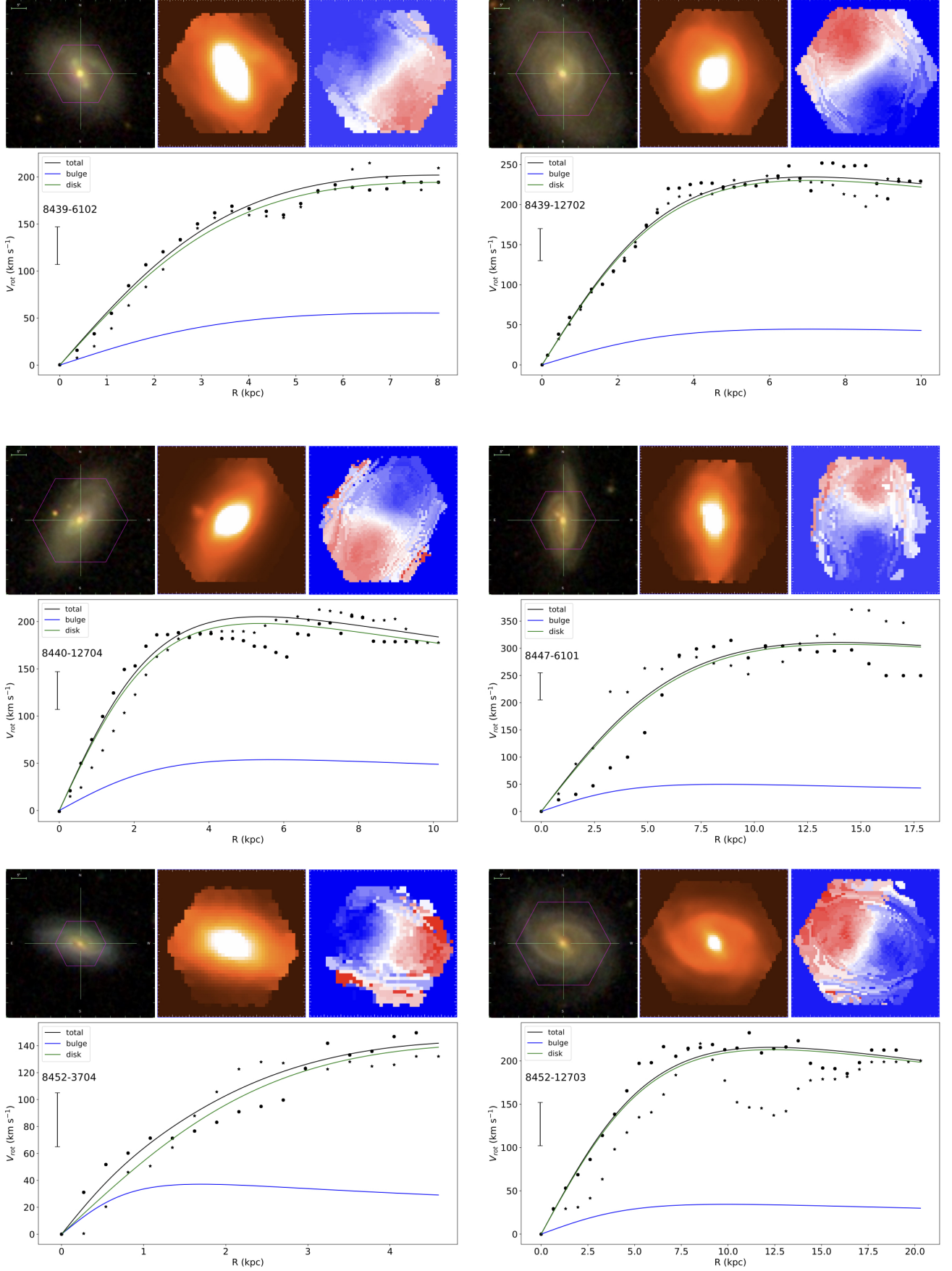


Figure A1. continued

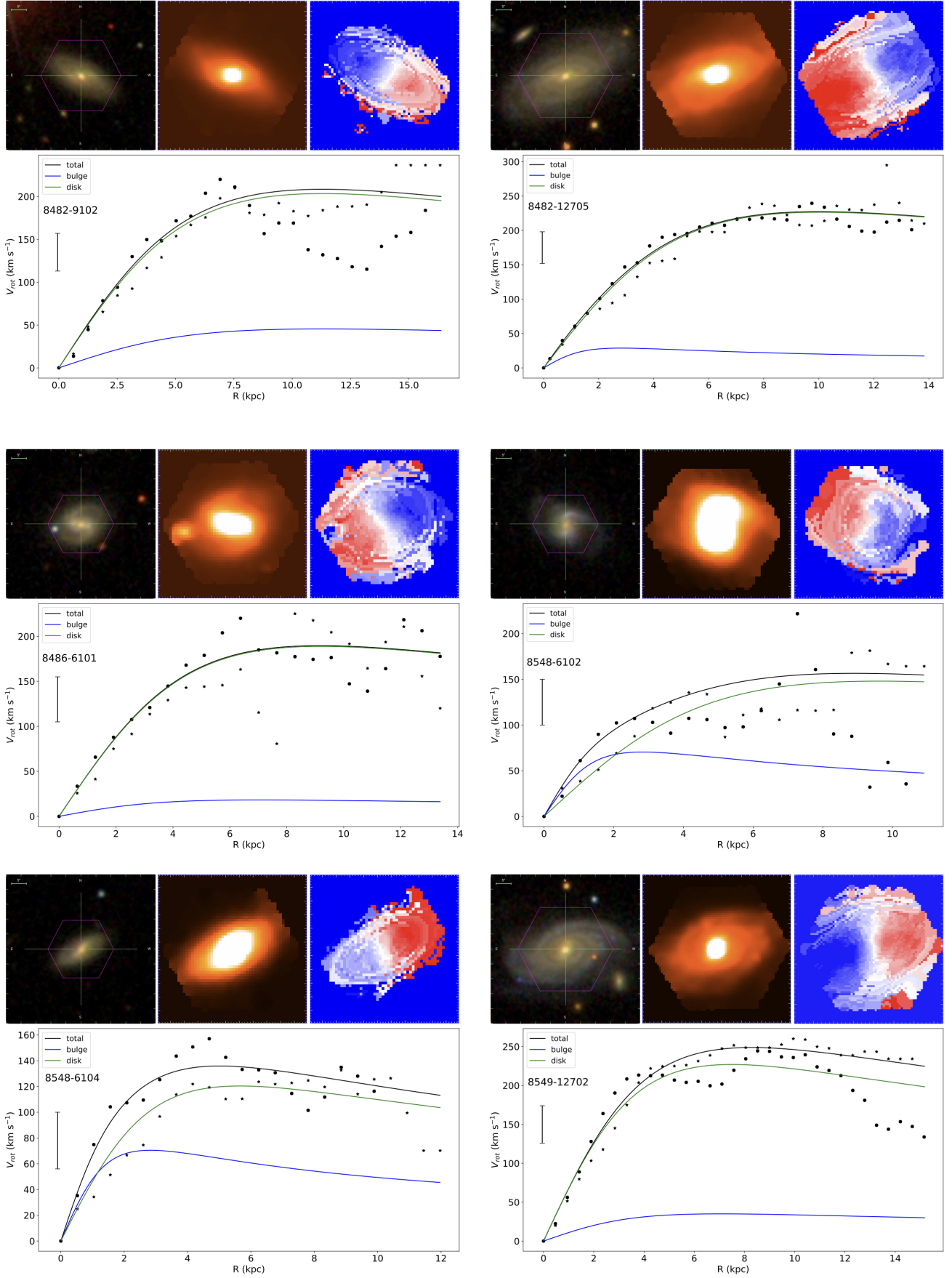


Figure A1. continued



**Table B1.** Dynamical parameters of the galaxies. Columns: (1) MaNGA ID; (2) stellar mass; (3) and (4) shape parameters and dynamical mass of the component 1 and 2 of the fitted Miyamoto–Nagai model, respectively; (5) maximum rotation velocity measured over each rotation curve; (6) total dynamical mass given by the sum of  $M_1$  and  $M_2$ . All data were obtained in Sect. 4. As mentioned in the text, errors in stellar masses are of  $\sim 1\%$ . These errors,  $V_{max}$ , and  $M_{dyn}$  errors only include uncertainties in our measurement process (see Sect. 4.3, 4.1, and 4.2 respectively for details).

Plate-IFU	$M_{star}/M_\odot$	Component 1	Component 2	$V_{max}$ (km s $^{-1}$ )	$M_{dyn}/M_\odot$
7495-12704	$8.04 \times 10^{10}$	$a_1 = 2.0$ kpc $b_1/a_1 = 1.00$ $M_1 = 5.0 \times 10^9 M_\odot$	$a_2 = 4.3$ kpc $b_2/a_2 = 0.39$ $M_2 = 1.4 \times 10^{11} M_\odot$	$205 \pm 7$	$(1.45 \pm 0.07) \times 10^{11}$
7962-12703	$2.25 \times 10^{11}$	$a_1 = 2.0$ kpc $b_1/a_1 = 1.00$ $M_1 = 3.0 \times 10^9 M_\odot$	$a_2 = 6.4$ kpc $b_2/a_2 = 0.38$ $M_2 = 3.4 \times 10^{11} M_\odot$	$255 \pm 13$	$(3.4 \pm 0.3) \times 10^{11}$
7990-3704	$2.08 \times 10^{10}$	$a_1 = 1.0$ kpc $b_1/a_1 = 1.00$ $M_1 = 1.5 \times 10^9 M_\odot$	$a_2 = 2.4$ kpc $b_2/a_2 = 0.37$ $M_2 = 2.5 \times 10^{10} M_\odot$	$117 \pm 7$	$(2.70 \pm 0.24) \times 10^{10}$
7990-9101	$2.47 \times 10^{10}$	$a_1 = 1.0$ kpc $b_1/a_1 = 1.00$ $M_1 = 1.0 \times 10^9 M_\odot$	$a_2 = 4.3$ kpc $b_2/a_2 = 0.58$ $M_2 = 7.0 \times 10^{10} M_\odot$	$132 \pm 8$	$(7.10 \pm 0.64) \times 10^{10}$
7992-6104	$3.59 \times 10^{10}$	$a_1 = 0.1$ kpc $b_1/a_1 = 1.00$ $M_1 = 3.0 \times 10^8 M_\odot$	$a_2 = 6.1$ kpc $b_2/a_2 = 0.57$ $M_2 = 3.6 \times 10^{11} M_\odot$	$221 \pm 11$	$(3.60 \pm 0.22) \times 10^{11}$
8082-6102	$8.02 \times 10^{10}$	$a_1 = 1.0$ kpc $b_1/a_1 = 1.00$ $M_1 = 8.0 \times 10^9 M_\odot$	$a_2 = 4.4$ kpc $b_2/a_2 = 0.36$ $M_2 = 1.7 \times 10^{11} M_\odot$	$221 \pm 9$	$(2.7 \pm 0.1) \times 10^{10}$
8083-6102	$1.29 \times 10^{11}$	$a_1 = 1.5$ kpc $b_1/a_1 = 1.00$ $M_1 = 5.0 \times 10^9 M_\odot$	$a_2 = 3.3$ kpc $b_2/a_2 = 0.32$ $M_2 = 1.2 \times 10^{11} M_\odot$	$220 \pm 9$	$(1.20 \pm 0.05) \times 10^{11}$
8083-12704	$3.66 \times 10^{10}$	$a_1 = 2.0$ kpc $b_1/a_1 = 1.00$ $M_1 = 1.0 \times 10^9 M_\odot$	$a_2 = 2.2$ kpc $b_2/a_2 = 0.59$ $M_2 = 3.7 \times 10^{10} M_\odot$	$134 \pm 8$	$(3.8 \pm 0.3) \times 10^{10}$
8133-3701	$2.44 \times 10^{10}$	$a_1 = 0.8$ kpc $b_1/a_1 = 1.00$ $M_1 = 4.0 \times 10^9 M_\odot$	$a_2 = 6.6$ kpc $b_2/a_2 = 0.48$ $M_2 = 2.0 \times 10^{11} M_\odot$	$173 \pm 12$	$(2.0 \pm 0.1) \times 10^{11}$
8134-6102	$6.06 \times 10^{10}$	$a_1 = 3.0$ kpc $b_1/a_1 = 1.00$ $M_1 = 6.0 \times 10^9 M_\odot$	$a_2 = 4.5$ kpc $b_2/a_2 = 0.33$ $M_2 = 2.5 \times 10^{11} M_\odot$	$266 \pm 8$	$(2.50 \pm 0.07) \times 10^{11}$
8137-9102	$4.34 \times 10^{10}$	$a_1 = 2.0$ kpc $b_1/a_1 = 1.00$ $M_1 = 6.0 \times 10^9 M_\odot$	$a_2 = 5.7$ kpc $b_2/a_2 = 0.40$ $M_2 = 1.5 \times 10^{11} M_\odot$	$178 \pm 5$	$(1.5 \pm 0.5) \times 10^{11}$
8140-12701	$4.53 \times 10^{10}$	$a_1 = 2.0$ kpc $b_1/a_1 = 1.00$ $M_1 = 6.0 \times 10^9 M_\odot$	$a_2 = 4.0$ kpc $b_2/a_2 = 0.35$ $M_2 = 6.0 \times 10^{10} M_\odot$	$144 \pm 5$	$(6.6 \pm 0.6) \times 10^{10}$
8140-12703	$1.07 \times 10^{11}$	$a_1 = 1.0$ kpc $b_1/a_1 = 1.00$ $M_1 = 3.0 \times 10^9 M_\odot$	$a_2 = 4.3$ kpc $b_2/a_2 = 0.53$ $M_2 = 1.5 \times 10^{11} M_\odot$	$199 \pm 6$	$(1.5 \pm 0.5) \times 10^{11}$
8243-6103	$5.83 \times 10^{10}$	$a_1 = 3.0$ kpc $b_1/a_1 = 1.00$ $M_1 = 4.0 \times 10^{10} M_\odot$	$a_2 = 3.5$ kpc $b_2/a_2 = 0.42$ $M_2 = 1.8 \times 10^{11} M_\odot$	$269 \pm 8$	$(2.2 \pm 0.1) \times 10^{11}$
8244-3703	$4.98 \times 10^{10}$	$a_1 = 2.0$ kpc $b_1/a_1 = 1.00$ $M_1 = 8.0 \times 10^9 M_\odot$	$a_2 = 5.4$ kpc $b_2/a_2 = 0.44$ $M_2 = 1.9 \times 10^{11} M_\odot$	$205 \pm 9$	$(1.90 \pm 0.06) \times 10^{11}$
8249-6101	$3.16 \times 10^{10}$	$a_1 = 1.5$ kpc $b_1/a_1 = 1.00$ $M_1 = 2.0 \times 10^9 M_\odot$	$a_2 = 2.5$ kpc $b_2/a_2 = 0.20$ $M_2 = 2.5 \times 10^{10} M_\odot$	$122 \pm 8$	$(2.7 \pm 0.2) \times 10^{10}$
8254-9101	$1.31 \times 10^{11}$	$a_1 = 0.5$ kpc $b_1/a_1 = 1.00$ $M_1 = 5.0 \times 10^9 M_\odot$	$a_2 = 4.8$ kpc $b_2/a_2 = 0.42$ $M_2 = 4.8 \times 10^{11} M_\odot$	$340 \pm 12$	$(4.8 \pm 0.1) \times 10^{11}$

Table B1 – continued

8256-6101	$3.40 \times 10^{10}$	$a_1 = 1.5$ kpc $b_1/a_1 = 1.00$ $M_1 = 7.0 \times 10^9 M_\odot$	$a_2 = 3.0$ kpc $b_2/a_2 = 0.33$ $M_2 = 7.6 \times 10^{10} M_\odot$	$188 \pm 6$	$(8.3 \pm 0.2) \times 10^{10}$
8257-3703	$5.92 \times 10^{10}$	$a_1 = 1.5$ kpc $b_1/a_1 = 1.00$ $M_1 = 3.0 \times 10^9 M_\odot$	$a_2 = 2.4$ kpc $b_2/a_2 = 0.33$ $M_2 = 4.8 \times 10^{10} M_\odot$	$163 \pm 5$	$(5.1 \pm 0.2) \times 10^{10}$
8257-6101	$3.67 \times 10^{10}$	$a_1 = 1.5$ kpc $b_1/a_1 = 1.00$ $M_1 = 3.0 \times 10^9 M_\odot$	$a_2 = 3.2$ kpc $b_2/a_2 = 0.31$ $M_2 = 5.7 \times 10^{10} M_\odot$	$155 \pm 9$	$(6.0 \pm 0.3) \times 10^{10}$
8312-12702	$6.59 \times 10^{10}$	$a_1 = 2.5$ kpc $b_1/a_1 = 1.00$ $M_1 = 3.0 \times 10^9 M_\odot$	$a_2 = 4.5$ kpc $b_2/a_2 = 0.40$ $M_2 = 1.2 \times 10^{11} M_\odot$	$180 \pm 6$	$(1.20 \pm 0.04) \times 10^{11}$
8312-12704	$3.58 \times 10^{10}$	$a_1 = 1.1$ kpc $b_1/a_1 = 1.00$ $M_1 = 2.8 \times 10^{10} M_\odot$	$a_2 = 8.0$ kpc $b_2/a_2 = 0.50$ $M_2 = 7.0 \times 10^{11} M_\odot$	$149 \pm 10$	$(9.8 \pm 0.9) \times 10^{10}$
8313-9101	$1.28 \times 10^{11}$	$a_1 = 1.7$ kpc $b_1/a_1 = 1.00$ $M_1 = 4.0 \times 10^{10} M_\odot$	$a_2 = 4.5$ kpc $b_2/a_2 = 0.40$ $M_2 = 1.5 \times 10^{11} M_\odot$	$236 \pm 7$	$(1.90 \pm 0.05) \times 10^{11}$
8317-12704	$2.33 \times 10^{11}$	$a_1 = 2.0$ kpc $b_1/a_1 = 1.00$ $M_1 = 1.0 \times 10^{10} M_\odot$	$a_2 = 6.0$ kpc $b_2/a_2 = 0.46$ $M_2 = 2.6 \times 10^{11} M_\odot$	$229 \pm 10$	$(2.7 \pm 0.2) \times 10^{11}$
8318-12703	$1.3 \times 10^{11}$	$a_1 = 2.0$ kpc $b_1/a_1 = 1.00$ $M_1 = 5.0 \times 10^{10} M_\odot$	$a_2 = 8.3$ kpc $b_2/a_2 = 0.44$ $M_2 = 2.4 \times 10^{11} M_\odot$	$214 \pm 9$	$(2.90 \pm 0.09) \times 10^{10}$
8320-6101	$3.79 \times 10^{10}$	$a_1 = 1.1$ kpc $b_1/a_1 = 1.00$ $M_1 = 1.0 \times 10^{10} M_\odot$	$a_2 = 3.2$ kpc $b_2/a_2 = 0.25$ $M_2 = 6.6 \times 10^{10} M_\odot$	$183 \pm 5$	$(7.6 \pm 0.3) \times 10^{10}$
8326-3704	$1.34 \times 10^{10}$	$a_1 = 2.5$ kpc $b_1/a_1 = 1.00$ $M_1 = 3.0 \times 10^9 M_\odot$	$a_2 = 4.0$ kpc $b_2/a_2 = 0.50$ $M_2 = 7.0 \times 10^{10} M_\odot$	$128 \pm 4$	$(7.3 \pm 0.4) \times 10^{10}$
8326-6102	$1.72 \times 10^{11}$	$a_1 = 1.5$ kpc $b_1/a_1 = 1.00$ $M_1 = 7.0 \times 10^9 M_\odot$	$a_2 = 5.0$ kpc $b_2/a_2 = 0.20$ $M_2 = 1.0 \times 10^{11} M_\odot$	$175 \pm 12$	$(1.00 \pm 0.07) \times 10^{11}$
8330-12703	$3.53 \times 10^{10}$	$a_1 = 1.5$ kpc $b_1/a_1 = 1.00$ $M_1 = 7.0 \times 10^9 M_\odot$	$a_2 = 5.2$ kpc $b_2/a_2 = 0.19$ $M_2 = 9.0 \times 10^{10} M_\odot$	$165 \pm 13$	$(9.7 \pm 0.9) \times 10^{10}$
8335-12701	$1.25 \times 10^{11}$	$a_1 = 3.5$ kpc $b_1/a_1 = 1.00$ $M_1 = 9.0 \times 10^9 M_\odot$	$a_2 = 6.0$ kpc $b_2/a_2 = 0.33$ $M_2 = 2.2 \times 10^{11} M_\odot$	$218 \pm 12$	$(2.2 \pm 0.1) \times 10^{11}$
8439-6102	$1.06 \times 10^{11}$	$a_1 = 2.7$ kpc $b_1/a_1 = 1.00$ $M_1 = 1.0 \times 10^{10} M_\odot$	$a_2 = 4.0$ kpc $b_2/a_2 = 0.42$ $M_2 = 1.3 \times 10^{11} M_\odot$	$202 \pm 6$	$(1.40 \pm 0.04) \times 10^{11}$
8439-12702	$6.05 \times 10^{10}$	$a_1 = 2.5$ kpc $b_1/a_1 = 1.00$ $M_1 = 6.0 \times 10^9 M_\odot$	$a_2 = 4.0$ kpc $b_2/a_2 = 0.25$ $M_2 = 1.6 \times 10^{11} M_\odot$	$235 \pm 7$	$(1.60 \pm 0.05) \times 10^{11}$
8440-12704	$5.17 \times 10^{10}$	$a_1 = 2.0$ kpc $b_1/a_1 = 1.00$ $M_1 = 7.0 \times 10^9 M_\odot$	$a_2 = 2.8$ kpc $b_2/a_2 = 0.35$ $M_2 = 9.0 \times 10^{10} M_\odot$	$205 \pm 6$	$(9.7 \pm 0.3) \times 10^{10}$
8447-6101	$3.66 \times 10^{11}$	$a_1 = 3.0$ kpc $b_1/a_1 = 1.00$ $M_1 = 9.0 \times 10^9 M_\odot$	$a_2 = 7.2$ kpc $b_2/a_2 = 0.39$ $M_2 = 5.7 \times 10^{11} M_\odot$	$312 \pm 14$	$(5.7 \pm 0.3) \times 10^{11}$
8452-3704	$1.84 \times 10^{10}$	$a_1 = 0.6$ kpc $b_1/a_1 = 1.00$ $M_1 = 1.0 \times 10^9 M_\odot$	$a_2 = 3.0$ kpc $b_2/a_2 = 0.33$ $M_2 = 4.8 \times 10^{10} M_\odot$	$142 \pm 4$	$(4.9 \pm 0.2) \times 10^{10}$

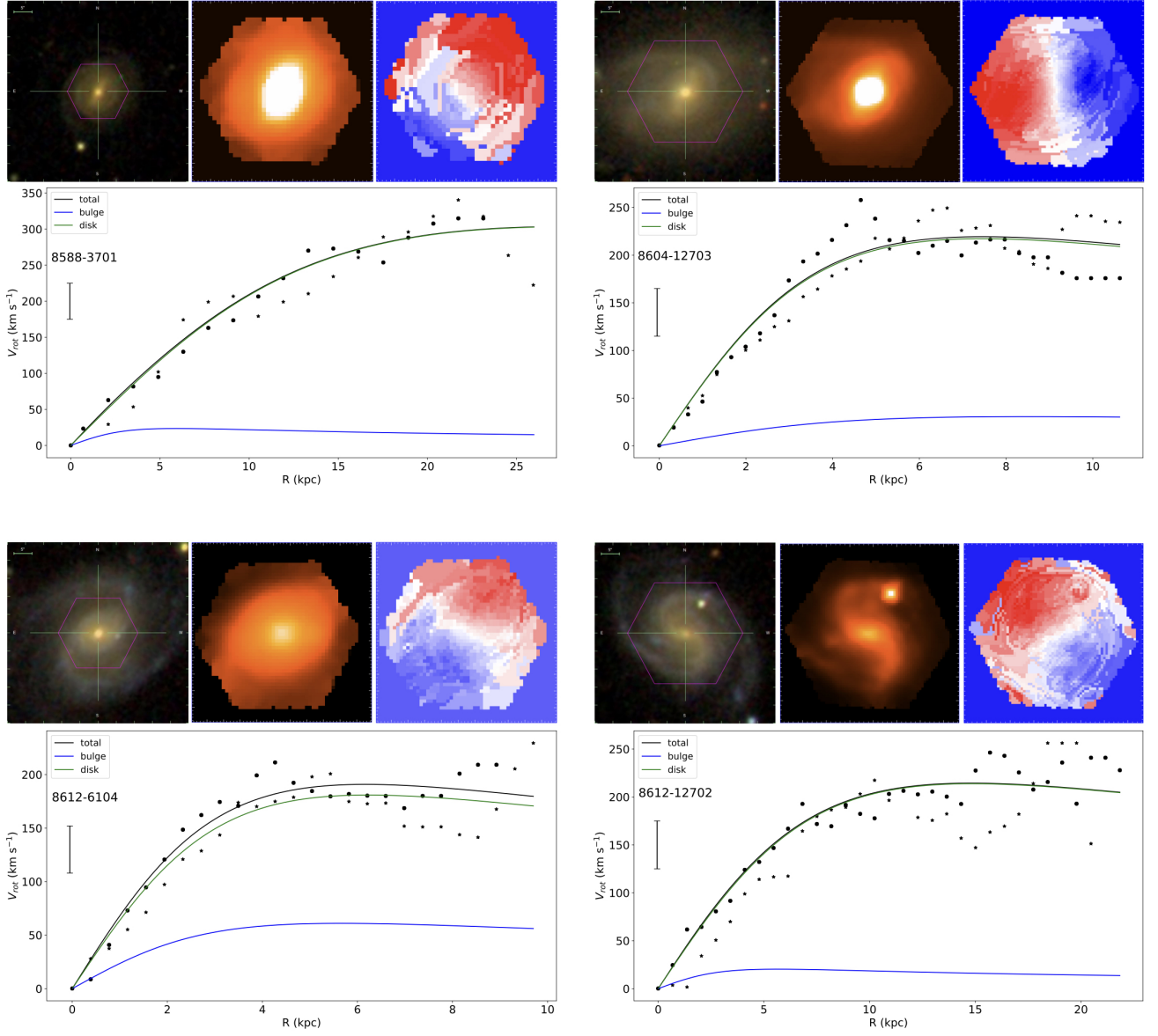


Figure A1. continued

**Table B1** – *continued*

8452-12703	$2.25 \times 10^{11}$	$a_1 = 3.5$ kpc $b_1/a_1 = 1.00$ $M_1 = 5.0 \times 10^9 M_\odot$	$a_2 = 6.1$ kpc $b_2/a_2 = 0.44$ $M_2 = 2.4 \times 10^{11} M_\odot$	$216 \pm 11$	$(2.4 \pm 0.1) \times 10^{11}$
8482-9102	$9.51 \times 10^{10}$	$a_1 = 4.0$ kpc $b_1/a_1 = 1.00$ $M_1 = 1.0 \times 10^{10} M_\odot$	$a_2 = 5.5$ kpc $b_2/a_2 = 0.45$ $M_2 = 2.0 \times 10^{11} M_\odot$	$208 \pm 15$	$(2.1 \pm 0.2) \times 10^{11}$
8482-12705	$1.26 \times 10^{11}$	$a_1 = 1.0$ kpc $b_1/a_1 = 1.00$ $M_1 = 1.0 \times 10^9 M_\odot$	$a_2 = 5.0$ kpc $b_2/a_2 = 0.42$ $M_2 = 2.2 \times 10^{11} M_\odot$	$227 \pm 7$	$(2.20 \pm 0.05) \times 10^{11}$
8486-6101	$1.12 \times 10^{11}$	$a_1 = 2.5$ kpc $b_1/a_1 = 1.00$ $M_1 = 1.0 \times 10^9 M_\odot$	$a_2 = 5.0$ kpc $b_2/a_2 = 0.30$ $M_2 = 1.4 \times 10^{11} M_\odot$	$189 \pm 11$	$(1.40 \pm 0.07) \times 10^{11}$
8548-6102	$2.69 \times 10^{10}$	$a_1 = 1.0$ kpc $b_1/a_1 = 1.00$ $M_1 = 6.0 \times 10^9 M_\odot$	$a_2 = 4.4$ kpc $b_2/a_2 = 0.54$ $M_2 = 9.0 \times 10^{10} M_\odot$	$155 \pm 9$	$(9.6 \pm 0.5) \times 10^{10}$
8548-6104	$6.04 \times 10^{10}$	$a_1 = 1.0$ kpc $b_1/a_1 = 1.00$ $M_1 = 6.0 \times 10^9 M_\odot$	$a_2 = 3.0$ kpc $b_2/a_2 = 0.33$ $M_2 = 3.5 \times 10^{10} M_\odot$	$136 \pm 6$	$(4.10 \pm 0.15) \times 10^{10}$
8549-12702	$1.61 \times 10^{11}$	$a_1 = 2.6$ kpc $b_1/a_1 = 1.00$ $M_1 = 6.0 \times 10^{10} M_\odot$	$a_2 = 4.5$ kpc $b_2/a_2 = 0.36$ $M_2 = 1.6 \times 10^{11} M_\odot$	$249 \pm 7$	$(2.20 \pm 0.07) \times 10^{11}$
8588-3701	$2.86 \times 10^{11}$	$a_1 = 2.1$ kpc $b_1/a_1 = 1.00$ $M_1 = 1.4 \times 10^9 M_\odot$	$a_2 = 12.9$ kpc $b_2/a_2 = 0.53$ $M_2 = 1.1 \times 10^{12} M_\odot$	$303 \pm 9$	$(1.10 \pm 0.04) \times 10^{12}$
8604-12703	$1.10 \times 10^{11}$	$a_1 = 3.0$ kpc $b_1/a_1 = 1.00$ $M_1 = 3.4 \times 10^9 M_\odot$	$a_2 = 3.6$ kpc $b_2/a_2 = 0.24$ $M_2 = 1.5 \times 10^{11} M_\odot$	$220 \pm 9$	$(1.50 \pm 0.06) \times 10^{11}$
8612-6104	$7.90 \times 10^{10}$	$a_1 = 2.0$ kpc $b_1/a_1 = 1.00$ $M_1 = 9.0 \times 10^9 M_\odot$	$a_2 = 3.2$ kpc $b_2/a_2 = 0.37$ $M_2 = 8.7 \times 10^{10} M_\odot$	$190 \pm 8$	$(9.6 \pm 0.4) \times 10^{10}$
8612-12702	$3.06 \times 10^{11}$	$a_1 = 2.0$ kpc $b_1/a_1 = 1.00$ $M_1 = 1.0 \times 10^9 M_\odot$	$a_2 = 7.0$ kpc $b_2/a_2 = 0.50$ $M_2 = 2.9 \times 10^{11} M_\odot$	$214 \pm 11$	$(2.9 \pm 0.2) \times 10^{11}$